Designing Nanomaterial-infused Working Fluids for Energy Efficiency Improvement in Microstructured Copper Heat Absorbers

Article history:
Received : 30.10.2025
Revised : 29.01.2026
Accept : 20.03.2026
Published : 09.07.2026

Wasurat Bunpheng[a], V. M. Rajavel Muthaiah[b], Ratchagaraja Dhairiyasamy[c], Deekshant Varshney[d], Subhav Singh[e], Choon Kit Chan[f*]

[a] Faculty of Engineering and Technology, Shinawatra University, Pathum Thani, Thailand

[b] University School of Automation & Robotics (USAR), Guru Gobind Singh Indraprastha University, East Campus, New Delhi, India

[c] Saveetha School of Engineering, Department of Electronics and Communication Engineering, Saveetha Institute of Medical and Technical Sciences, Saveetha University, Chennai, Tamil Nadu, India

[d] Centre of Research Impact and Outcome, Chitkara University, Rajpura, Punjab, India

[e] Chitkara Centre for Research and Development, Chitkara University, Himachal Pradesh, India

[f] Faculty of Engineering and Quantity Surveying, INTI International University, Nilai, Negeri Sembilan, Malaysia

***Corresponding Author's Email**
ratchagaraja@gmail.com

Abstract: Passive solar-thermal systems depend on efficient heat transfer to keep absorber temperatures low. Nanofluid working media and microstructured copper interfaces can intensify boiling and rewetting using passive modifications. Integrated, stability-screened comparisons that combine nanofluids with fabricated microstructures under unified boundary conditions remain limited. This study quantifies the coupled influence of nanofluid formulation and copper surface topology on passive phase-change devices. Graphene, CuO, Al_2O_3, and TiO_2 nanofluids (0.05–0.30 wt%) were prepared and characterized for dispersion size, zeta potential, UV–Vis retention, viscosity, and thermal conductivity, and were tested in circular and flat-plate wicked heat pipes and a wickless thermosyphon with plain, hemispherical, and micropillar evaporators from 20–100 W at 0°–90° with triplicate repeats (k=2). Micropillar evaporators exhibit low resistance; the maximum reduction was 48% compared with plain copper, indicating enhanced capillary replenishment and wetted area. Graphene provides the strongest fluid effect; at 100 W on micropillars in the circular device, the thermal resistance fell from 0.210 to 0.168 °C/W, supporting coupled conductivity and interfacial conditioning. These quantified gains support absorber-interface redesign for higher energy efficiency and reduced orientation sensitivity. Future work targets long-cycle durability, fouling, and outdoor exposure of nanomaterial suspensions.

Keywords: Energy efficiency, nanomaterial, graphene nanofluid, micropillar copper surface, thermal resistance reduction

1. INTRODUCTION

Solar-thermal technologies depend on the efficient transfer of absorbed irradiance into a useful heat stream while keeping absorber temperatures low enough to limit thermal losses and maintain material durability. Flat-plate solar collectors remain widely deployed because fabrication is simple to fabricate, integration into the footprint is practical, and operation can be maintained with simple hydraulics. Performance in these systems is frequently constrained by the modest thermophysical properties of conventional working fluids and by interfacial resistances at the absorber–fluid interface, particularly under low mass flow in natural circulation intermittently reduced insolation (Elumalai & Kadamban, 2025). Water-based media are commonly used because of their favourable cost and safety, yet thermal conductivity remains limited (on the order of 0.6 W m^{-1} K^{-1} near room temperature), and glycol mixtures used for freeze protection exhibit evener conductivity and higher viscosity (Nallusamy & Rathinasamy, 2025). Under these conditions, a higher absorber–fluid temperature difference is often required to sustain a given heat rate, and this requirement can increase radiative and convective losses from the collector envelope while accelerating degradation mechanisms, such as scaling and corrosion at hot spots.

Working-fluid modification through nanofluids has been investigated as a route to increase effective thermal conductivity and to alter near-wall transport during convection and boiling. Nanofluids are commonly defined as colloidal suspensions of nanoscale solids dispersed in a base liquid, and enhanced thermal transport has been attributed to high intrinsic particle conductivity, interfacial heat transfer, and micro convection effects under appropriate dispersion conditions. Earlier studies have reported efficiency improvements in solar collectors and reduced thermal resistance in heat pipes when oxides (e.g., Al_2O_3, TiO_2, CuO) or carbon nanomaterials (e.g., graphene, nanotubes) were dispersed in water. In many such investigations, performance gains were reported alongside increased viscosity, and long-term operation was limited by agglomeration, sedimentation, and deposition on heat-transfer surfaces (Darvesh et al., 2025). These practical constraints have placed emphasis on stability diagnostics such as hydrodynamic size distributions, zeta potential, and optical absorbance evolution, since clogging of narrow passages, drift in thermal conductivity, and sustained viscosity growth represent realistic barriers to field deployment.

Surface micro structuring has also been advanced as a passive method to intensify interfacial heat transfer in copper absorbers and evaporators. Microstructures can increase the density of stable nucleation sites, modify wettability and contact-line dynamics, and promote thin-film replenishment by capillary pathways when liquid return is required. Feature families based on cavities and pillars have been repeatedly adopted because they represent two physically distinct mechanisms: hemispherical cavities can act as persistent vapor entrapment sites and activate nucleation at lower superheat, while micropillars can create interconnected capillary lanes that support rewetting and microlayer renewal. Copper is particularly suitable for these approaches because micromachining, texturing, and selective etching can be applied without compromising bulk conductivity, and the resulting patterns can be scaled toward absorber manufacturing routes (Soudagar et al., 2025). Despite these motivations, surface-focused studies have often been conducted with a single working fluid and limited property screening, thereby restricting the attribution of measured gains to topology alone.

The surveyed works (Table 1) showed that dispersions containing graphene or MWCNTs delivered the largest conductivity and HTC gains, as well as shortened start-up times, while oxide nanofluids strengthened capillary limits and reduced wall temperatures, accompanied by smaller viscosity increases. Studies that tuned orientation, fill ratio, and device architecture reported larger improvements than studies that varied fluid alone, which reinforced the premise that fluid formulation must be coordinated with geometry and operating angle (Jin et al., 2025). Evidence from photovoltaic and solar-collector platforms indicated that nanofluid improvements propagated to electrical output and storage capacity, thereby motivating the present cross-geometry, angle-resolved experiments with structured evaporators and carefully conditioned graphene and oxide suspensions (Dhairiyasamy et al., 2025).

A central unresolved issue has been the scarcity of experimental studies that simultaneously evaluate nanofluid formulation, stability validation, rheology control, and fabricated microstructured copper interfaces under a single set of controlled boundary conditions. Much of the literature has tested nanofluids on fixed, untextured surfaces or on surfaces with a fixed base fluid, leaving coupled interactions insufficiently resolved (Chakraborty & Chakraborty, 2025). Even when both levers were considered, dispersion screening and acceptance criteria were not consistently enforced prior to charging, and device-to-device variations in geometry, heat input definitions, condenser conditions, or inclination protocols were often introduced. Such heterogeneity has limited the ability to decouple fluid effects from surface effects and has reduced the comparability of reported thermal-resistance reductions across studies. These limitations are reflected in the evidence base summarized in Table 1, where representative reports have frequently emphasized either fluid enhancement or interface structuring, while integrated matrices spanning dispersion stability metrics, rheological constraints, and microstructured copper geometries have remained limited (K et al., 2025).

 https://doi.org/10.37819/nanofab.2025.0019

Table 1. Nanofluid- and structure-enhanced heat pipes and related

Objective / Aim	Methodology / Approach	Materials / Parameters	Key Findings / Results	Relevance to Current Study
LHP cooling for bifacial PV	Irradiance tests; RSM optimization	Al_2O_3, CuO, TiO_2, MWCNT, Al_2O_3–CuO, TiO_2–MWCNT; 600–1000 W m^{-2}; fill, conc, tilt	TiO_2–MWCNT k=0.760; rear T −47.7%; η_{elec} +20.4%; opt 1.3 vol%, 78%, 50°	Reinforces angle effects; supports hybrid screening (Hu et al., 2025)
PV/TEG with nanofluid flat HP	Modeling + experiments	FP heat pipe; Ag 5 vol% vs water; irradiance, condenser T	Output 1.82 W at 10,000 W m^{-2}; energy/exergy ↑ with Ag	Supports FPHP relevance; motivates high-k fluids (Gao et al., 2022)
Heat-pipe nanofluid gains	Controlled tests + property work	Ag, Al_2O_3, MWCNT; conc, fill, tilt; $R_{th,}$ HTC	Ag: k +150%; R_{th} −83%; HTC +300%; best 70% fill, 30°	Guides fill/tilt choices; supports R_{th} focus (Govindasamy et al., 2025)
Nanofluid PHP start-up	3-turn PHP; visualization	PbS/H_2O, Au/H_2O, Graphene/H_2O; ≤1.0 wt%; 80% fill; 60°	Start-up time ↓; heat transfer ↑; graphene best	Supports graphene for nucleation/start-up (Hu et al., 2025)
HP-assisted thermal storage	Outdoor PTC + storage	Al_2O_3/soybean oil; KNO_3–$NaNO_3$ PCM; natural-circulation TS	Storage capacity +67%	Links nanofluids to system integration/storage (Kalbande et al., 2022)
OHP battery thermal mgmt	BTMS tests (1C–2C)	Al_2O_3, graphene, MWCNT; water/ acetone; 0.25–0.5 wt%; 35 °C	Acetone-MWCNT 0.25 wt%: cell T −7.5 to −11 °C; spread −2.0 to −2.7 °C	Shows carbon benefit; base-fluid choice matters (Kumar et al., 2025)
Vibration effects in PHP	~30 Hz vibration tests	CuO+Fe_3O_4/water 2 wt%; tilt; vib on/off	Start-up T ↓; R_{th} −13.49%; vib adds −8 to −11%	Suggests excitation mitigates low-angle limits (Mane et al., 2025)
Grooved CHP with nanofluids	Correlation-based model	CuO/H_2O, Al_2O_3/H_2O; conc; horiz; heat-sink T	Capillary limit +25% (CuO), +14% (Al_2O_3); R_{th} −68% (CuO), −51% (Al_2O_3); T_{wall} −24% (CuO)	Mechanistic support for capillary/R_{th} metrics (Saad et al., 2022)
Solar tube collectors + graphene	Experiments + stability checks	Graphene/DI 0.1–0.3 vol%; 1.5–4.5 L min^{-1}; SEM/XRD; ζ (30 d)	ΔT +52.94% at 4.5 L min^{-1}; performance +41.3%; water ~25% lower	Supports graphene stability + collector gains (Thanikodi et al., 2025)
Gravity HP start-up (graphene)	Property + start-up tests	Graphene/H_2O 0.05 wt% + PVP; 30, 60 W	Start-up time −15.1% (30 W), −10.7% (60 W)	Supports low-dose graphene for start-up (Zhao et al., 2018)

The motivation for focusing on flat-plate collectors arises from the combination of widespread deployment and persistent thermal bottlenecks associated with conventional fluids and planar absorber interfaces. While evacuated-tube systems and concentrating collectors have been deployed for higher-temperature applications, flat-plate collectors continue to dominate low-to-moderate-temperature applications in buildings and process heating, where cost, reliability, and ease of installation are decisive. Improvements at the absorber–fluid interface are therefore valuable because they can reduce the required absorber temperature for a given heat delivery rate, thereby decreasing thermal loss drivers without altering the collector form factor (Chan et al., 2024). Insights from heat-pipe and PVassisted thermal management studies are directly relevant because the governing limitation frequently resides at the evaporator boundary, where interfacial transport, wetting, and capillary supply determine the required wall superheat. Evaporator-focused performance metrics developed in heat-pipe studies can be translated into absorber design principles for flat plates when embedded heat spreaders, vapor chambers, or passive phase-change modules are integrated beneath planar absorber footprints, and when orientation sensitivity must be managed in roof-mounted installations (Kadirgama et al., 2025).

The present study has been positioned to resolve the coupled role of working-fluid formulation and microstructured copper topology through a unified experimental platform in which variables were decoupled by design. Nanofluid families based on graphene, CuO, Al_2O_3, and TiO_2 were prepared under a standardized protocol, and charging was conditioned on stability and property screening using dynamic light scattering, zeta potential, UV–Vis absorbance tracking, viscosity–shear characterization, and thermal conductivity measurement. Copper surfaces were fabricated in three representative states—plain, hemispherical, and micropillar—so that a cavity-dominated nucleation archetype and a capillary-lane archetype were both tested under consistent metrology and cleaning/conditioning procedures. Boundary conditions were standardized through a common heating and cooling framework and fixed inclination settings, and the evaluation was extended across three device geometries that map onto practical passive heat-transfer implementations: a circular wicked heat pipe, a flat-plate heat pipe aligned with planar absorber footprints, and a wickless thermosyphon representing gravity-assisted return. This structure allowed main effects to be isolated by holding all but one factor constant within each comparison block and coupled interactions to be examined through systematic pairing of the same fluid set with the same surface set under the same operating protocol.

The objective of this study was to quantify, under standardized boundary conditions and stability-qualified working fluids, the independent and combined influences of nanofluid formulation and copper surface microstructure on passive thermal-transport performance across circular, flat-plate, and wickless phase-change devices relevant to flat-plate solar-thermal collector integration.

2. MATERIALS AND METHODS

Materials were designed to enable defensible justification of device selection, transparent normalization across geometries, and reproducible isolation of fluid and surface effects under controlled boundary conditions. Three device geometries were tested because a curved wick-assisted format, a planar wick-assisted format, and a wickless gravity-assisted format each represented widely used passive heat-transport archetypes, and because each archetype imposed distinct constraints on liquid return, vapor-core confinement, and orientation dependence relevant to solar-thermal integration scenarios. A circular heat pipe (CHP), a flat-plate heat pipe (FPHP), and a wickless thermosyphon (TS) were fabricated from oxygen-free copper, and each device was configured with a dedicated evaporator region prepared as a copper heat-absorber surface. The same three surface variants were applied to the evaporator region of each geometry, so that geometry and surface-topology effects were not confounded by selective application. Cross-geometry comparison was enabled by defining all performance metrics on a common energetic basis using corrected heat input and explicitly defined reference temperatures and areas, and by reporting each metric using geometry-specific geometric factors recorded during fabrication metrology. Table 2 lists the primary device dimensions, wick attributes, and inventory settings carried into metric evaluation and uncertainty propagation, and constant fill ratios were retained within each geometry to isolate nanofluid material effects from inventory optimization effects.

Copper evaporator surfaces were prepared in three variants to represent a smooth baseline, a cavity-dominated topology, and a pillar-dominated topology using fabrication routes that supported repeatable feature dimensions. A plain condition was produced by controlled mechanical polishing, and the arithmetic roughness was measured as $R a = 0.30 \mu$musing profilometry performed on at least five non-overlapping 1×1 mm 2 tiles per specimen. Areal roughness parameters $S a$and $S q$ were computed from the same tiles for reporting consistency, and an area amplification factor ϕwas derived from profilometry to support consistent evaporator-area definitions during heat-transfer-coefficient evaluation. Hemispherical textures were produced by mask-guided micro-dimpling of copper evaporator substrates to form dome-like protrusions

 https://doi.org/10.37819/nanofab.2025.0019

Table 2. Device geometries, internal features, and inventory settings used for thermal testing and data reduction

Device type	Body material	Key fabricated dimensions	Internal feature definition	Inventory definition	Fill ratio
CHP	Oxygen-free copper	ID 6.0 mm; wall 0.8 mm; length 250 mm	Sintered copper powder wick; porosity 0.55–0.60; mean pore radius 10–20 μm	Charged volume referenced to evaporator volume	50 ± 2%
FPHP	Copper laminate	100 × 100 × 3.0 mm; vapor cavity 0.8 mm	Integral return pathways to perimeter condenser gallery	Charged volume referenced to evaporator volume	50 ± 2%
TS	Copper tube	ID 10.0 mm; length 300 mm	Wickless vapor core; tube-in-shell condenser connection	Charged volume referenced to evaporator volume	60 ± 2%

with nominal diameter 40 µm, pitch 80 µm, and depth 20 µm. Micropillar textures were fabricated by laser-assisted micromachining followed by selective etching to yield pillars with diameters of 30±3µm, heights of 50±5µm, and a pitch of 70 ± 5 µm in a square lattice. Feature dimensions were selected to maintain a characteristic spacing within a regime compatible with capillary-fed wetting films and nucleation-site density enhancement, while remaining manufacturable on copper at the evaporator footprint scale. Dimensional tolerances were quantified by scanning electron microscopy and profilometry before device charging. Oxygen-plasma cleaning was applied after machining to remove organic residue and standardize the initial surface energy, and a vapor-phase salinization treatment with a hydrophilic terminus and a short surfactant chain was applied only to the graphene-test set to stabilize platelet wetting and continuity along microstructured features. Wettability checks were performed on each surface condition using sessile-drop measurements with 5 µL droplets and syringe-controlled ramps of 1 µL s −1, and advancing and receding angles were recorded to document hysteresis induced by microstructural edges. To limit confounding from conditioning, plasma exposure time and power settings were retained across all surface variants within a device set, and silanization was treated as a controlled conditioning variable recorded as a method input rather than as a performance mechanism. Table 3 defines the microstructure parameters and the metrology outputs and inputs used for area normalization and surface-state documentation.

A modular thermal test bench was assembled to impose repeatable heating, condenser cooling, inclination control, and synchronized measurement across all devices. Figure 1 presents a schematic

Table 3. Evaporator surface variants, defining feature dimensions, and metrology outputs used for wettability and area normalization

Surface variant	Fabrication route	Defining dimensions	Roughness and area inputs used in analysis	Conditioning control
Plain	Mechanical polishing	R_a = 0.30 μm	S_a, S_q, ϕ from profilometry tiles	Oxygen-plasma cleaning
Hemispherical	Mask-guided micro-dimpling	Diameter *40 µm;* pitch *80 µm;* depth *20 µm*	S_a, S_q, ϕ from profilometry tiles	Oxygen-plasma cleaning
Micropillar	Laser micromachining + selective etch	Diameter 30 ± *3µm;* height 50 ± 5*µm;* pitch *70 ± 5µm*	S_a, S_q, ϕ from profilometry tiles	Oxygen-plasma cleaning; silanization recorded for graphene set

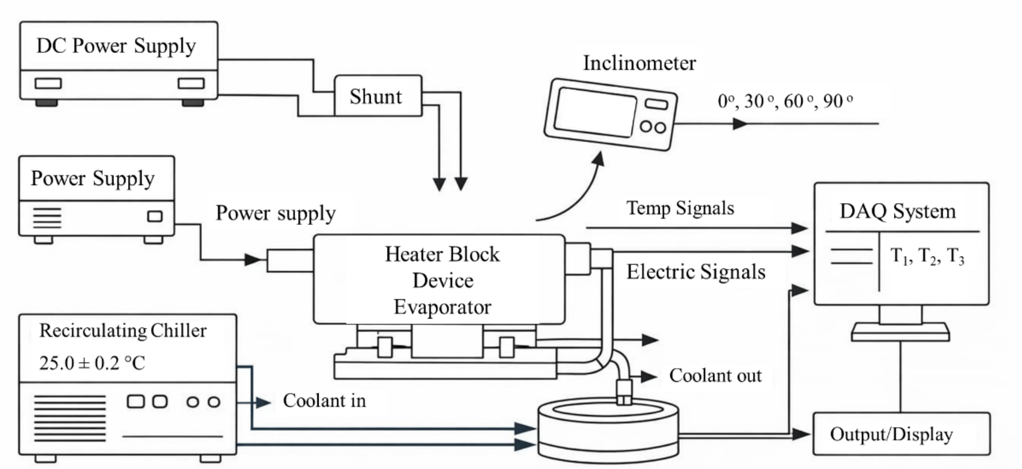

Figure 1. Schematic defining heating, cooling, inclination control, and synchronized acquisition used

in which the heater block, test article mount, condenser coolant loop, and data-acquisition routing were configured as a closed sequence to establish controlled boundary conditions. In the schematic, electrical power delivery was routed through an inline shunt used for current verification, and voltage was recorded at the heater terminals to support power calculation. A recirculating chiller was used to maintain coolant supply temperature at, and inlet and outlet coolant temperatures were recorded using calibrated thermistors embedded in inline tees. A goniometric mounting stage equipped with an electronic inclinometer was used to set inclination angles of 0°, 30°, 60°, and 90°, with the selected angle spanning horizontal placement, common roof-tilt regimes, and vertical placement relevant to solar-thermal installation constraints and gravity-assisted return limits. Ambient conditions were controlled within a draft-shielded enclosure, and a transparent guard reduced radiative exchange with the laboratory. Detailed wiring maps, grounding architecture, and logger-channel assignment tables were archived as supplementary material to preserve traceability without expanding the main narrative.

Temperature sensing and measurement-plane definitions were standardized to support fair comparisons across geometries and to enable consistent selection of reference temperature for heat-transfer calculations. Figure 2 presents the sensor placement and defines the evaporator, adiabatic, and condenser measurement planes, along with the averaging rules used for each plane. K-type thermocouples meeting class-1 tolerances were bonded to outer walls at three evaporator locations, two adiabatic locations, and two condenser locations using silver-filled epoxy, and strain relief was applied to limit lead-induced drift. A curing protocol was applied to stabilize bond lines and reduce contact thermal resistance variability, and mounting jigs were used to place sensors at fixed offsets from geometric references, ensuring plane definitions remained consistent across devices. A sampling frequency of 2 Hz was used, and steady-state windows were selected only after the thermal slope and power stability criteria were satisfied. The evaporator mean wall temperature T_e was computed as the arithmetic mean of the three evaporator thermocouples, the condenser mean wall temperature T_c was computed as the arithmetic mean of the condenser thermocouples, and the coolant inlet temperature T_{in} was recorded at the condenser inlet tee and was used as the reference temperature T_{ref} for evaporator superheat and evaporator heat-transfer-coefficient evaluation.

Nanofluids were formulated and screened using a dispersion protocol selected to remain transferable across oxide nanoparticles and platelet-type graphene while maintaining acceptance thresholds aligned with common colloidal stability practice and operational constraints for passive devices. Figure 3 presents the formulation workflow and identifies the sequence used for each batch from pH conditioning through mixing, sonication, filtration, degassing, and pre-charge characterization. Commercial CuO, Al_2O_3, $TiOO_2$ (anatase), and few-layer graphene nanoplatelets were dispersed in deionized water at concentrations spanning 0.05–0.30 wt%, with the selected range used to avoid excessive viscosity elevation, filter plugging risk, and rapid sedimentation associated with higher loadings, while

 https://doi.org/10.37819/nanofab.2025.0019

Figure 2. Experimental rig, instrumentation, and wiring

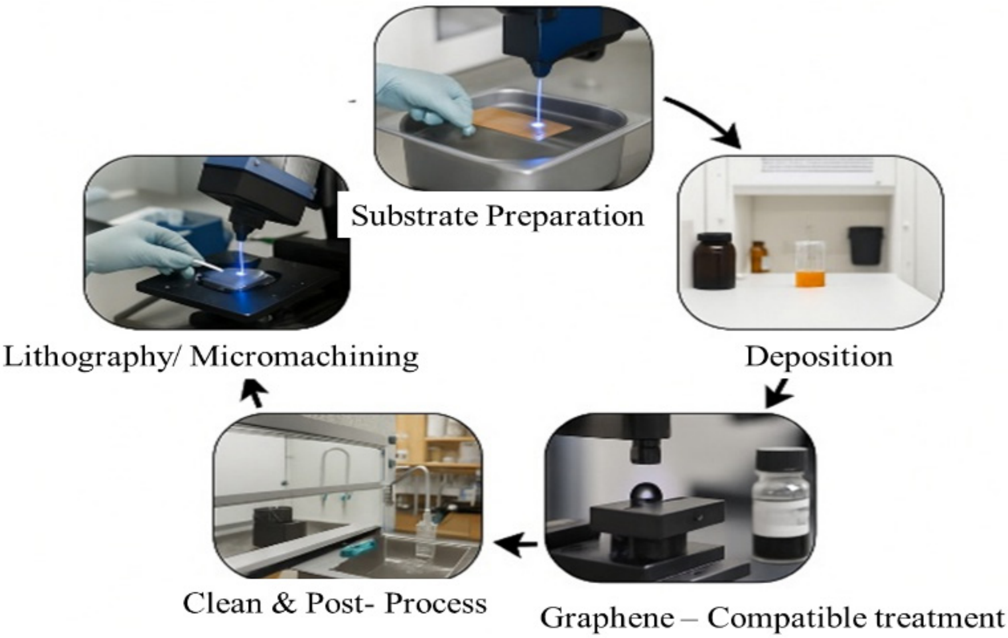

Figure 3. Nanofluid formulation, screening, and post-cycling verification workflow used for charge approval and property retention checks

still enabling measurable conductivity augmentation and stable electrostatic screening at low loading. The dispersion pH was adjusted to the 8–9 range using dilute ammonia; magnetic stirring was applied for 10 min, and probe sonication was applied for 30 min, with an ice bath used for temperature control. A 0.2 μm PTFE filtration step was used to remove large agglomerates, and vacuum degassing for 5 min was performed to limit dissolved gas content prior to filling. Acceptance criteria for device charging were defined to enforce dispersion stability and operational practicality, and thresholds were set as $|\zeta| \geq 30$ mVfor electrostatic stability, 24 h UV–Vis absorbance loss $\leq$ 15%for sedimentation screening, viscosity rise at a representative shear rate $\leq$ 10%relative to deionized water, and conductivity ratio at the selected concentration meeting the formulation target recorded for each fluid family. DLS particle-size distributions, zeta potential, UV–Vis absorbance retention, viscosity, and thermal conductivity were measured prior to charging and were rechecked after completion of the thermal-test campaign using companion aliquots sealed in vials and cycled through the same temperature-time program imposed during device testing so that property retention under cycling was documented without disturbing the charged devices. Table 4 lists characterization settings and acceptance thresholds used during screening and post-cycling verification.

Rheological characterization was performed under temperature-controlled conditions to address representativeness relative to evaporator operation and to provide inputs for uncertainty and screening logic. Viscosity was measured at 25 °C to match condenser-loop and laboratory boundary conditions used during charging, and temperature sweeps were executed across a bracket that included elevated temperatures consistent with evaporator wall temperatures encountered during heating. Shear-rate sweeps were executed up to $10^3\ s^{-1}$, and a representative shear rate of $100\ s^{-1}$was used for screening and comparison to enforce a consistent operational constraint. Thermal conductivity measurements were performed under controlled temperature to reduce drift, and repeated reads were acquired during both pre-charge screening and post-cycling verification. DLS measurements were conducted using a backscatter geometry at 173° with a 633 nm laser, and zeta potential was measured under controlled temperature and ionic conditions consistent with the pH-adjusted formulation. Table 5 lists the principal measurement systems, the calibration or verification steps retained for each, and the model identifiers and manufacturers, which were recorded in supplementary documentation to preserve traceability.

Thermal testing was conducted in a fixed sequence to ensure a fair comparison across fluids, surfaces, and geometries. Heat input was applied in discrete steps spanning the operating range used in the study, and each step was maintained until steady-state criteria were met. A steady-state window was accepted only when the absolute slope of each wall-temperature trace remained below $0.05\ ^{\circ C}\ min^{-1}$ for at least 10 min, and when electrical power drift remained below 0.2%, the acquisition was continued for at least 12 min for averaging. Three independent repeats were performed for each unique configuration defined by geometry, surface topology, working fluid, inclination angle, and heat-input level, and each repeat was initiated after re-equilibration at the set inclination. Tests affected by unstable boiling or intermittent dry-out were identified using objective exclusion criteria, and any run was rejected if a sustained step-like rise in T_e exceeding 5 K occurred at fixed Q, if quasi-periodic oscillations exceeding 2 K peak-to-peak persisted for longer than 120 s within the averaging window, or if the steady-state slope criterion was not satisfied within a maximum stabilization time fixed for the campaign. Excluded conditions were repeated under identical settings until three valid repeats were obtained or until stability could not be achieved under the fixed boundary conditions.

Table 4. Nanofluid screening metrics, acceptance thresholds, and recheck plan used for charge approval and cycling verification

Metric	Symbol	Screening method	Acceptance threshold / rule	Recheck condition
Zeta potential	ζ	Electrophoretic mobility		ζ
Optical retention	A/A_0	UV–Vis absorbance	$24\ h$ loss ≤ 15%	After campaign via cycled companion aliquot
Size distribution	—	DLS intensity PSD	Modal size recorded for traceability	After campaign via cycled companion aliquot
Viscosity rise	$\Delta\mu/\mu$	Rheometry	≤ 10% at fixed $\dot{\gamma}$	After campaign via cycled companion aliquot
Conductivity ratio	k/k_{DI}	Conductivity probe	Formulation target recorded per batch	After campaign via cycled companion aliquot

 https://doi.org/10.37819/nanofab.2025.0019

Table 5. Instrument classes and calibration or verification steps used for reproducible measurements

Measurement	Instrument class	Verification or calibration step retained
Wall temperature	K-type thermocouples	Calibration residuals recorded; bonding protocol standardized
Coolant temperatures	Calibrated thermistors	Two-point verification against reference thermometer
Electrical input	Shunt + 6½-digit multimeter	Shunt factor verification; voltage at terminals recorded
Inclination	Inclinometer on goniometer	Angle zeroing and repeatability check at setpoints
DLS	Backscatter DLS system	Standard check dispersion used for instrument sanity check
Zeta potential	Electrophoretic mobility system	Conductivity and cell checks recorded
UV–Vis	Spectrophotometer	Baseline and cuvette repeatability checks retained
Viscosity	Temperature-controlled rheometer	Temperature stability check and viscosity standard check
Conductivity	Conductivity probe method	Reference fluid check at test temperature

Data reduction was performed with explicit metric definitions selected to support cross-geometry normalization and to isolate surface and fluid effects. Electrical input power Q_{el} was computed from measured voltage V and current I as expressed in Equation (1), and corrected heat input Q was computed using a loss fraction η_{loss} as expressed in Equation (2). In Equation (2), η_{loss} was obtained from a combined model-and-calibration procedure that used radiative and parasitic estimates anchored by an independent coolant enthalpy balance executed during validation runs. Coolant heat removal Q_{cool} was computed from measured mass flow rate $\dot{m}$, coolant heat capacity c_p, and measured inlet and outlet temperatures T_{in} and T_{out} as expressed in Equation (11), and η_{loss} was adjusted during validation so that Q matched Q_{cool} within the combined measurement uncertainty.

$$Q_{el} = VI \quad (1)$$

$$Q = Q_{el}(1 - \eta_{loss}) \quad (2)$$

$$Q_{cool} = \dot{m} c_p \left(T_{out} - T_{in} \right) \quad (11)$$

Thermal resistance R_{th} was computed from T_e, T_c, and Q as expressed in Equation (3). Evaporator superheat ΔT_e was defined using the reference temperature $T_{ref} = T_{in}$ as expressed in Equation (4), and T_{ref} was selected because it represented a stable boundary condition tied to condenser cooling control and avoided dependence on spatially varying wall temperatures. The evaporator heat transfer coefficient h was computed as expressed in Equation (5) using a projected evaporator planform area A_{proj} so that h comparisons remained consistent across surfaces without embedding microstructure surface-area amplification into the denominator. A microstructure area factor ϕ was recorded from profilometry, and an effective wetted area A_e was defined as expressed in Equation (12) for secondary analyses in which microstructure area scaling was required. The effective thermal conductivity k_{eff} was computed as expressed in Equation (6) using an axial spacing L between evaporator and condenser mean planes and a geometry-specific cross-sectional area A_{cs}, and the formulation was treated as a one-dimensional axial index. For the flat-plate device, the k_{eff} calculation was applied using the defined axial spacing between mean planes and the corresponding cross-sectional area normal to axial transport, and lateral spreading effects were treated as outside the scope of the one-dimensional index.

$$R_{th} = \frac{T_e - T_c}{Q} \quad (3)$$

$$\Delta T_e = T_e - T_{\mathrm{ref}}, T_{\mathrm{ref}} = T_{in} \quad (4)$$

$$h = \frac{Q}{A_{proj}\Delta T_e} \quad (5)$$

$$A_e = \phi A_{proj} \quad (12)$$

$$k_{eff} = \frac{L}{A_{cs}R_{th}} \quad (6)$$

Orientation sensitivity was quantified using a normalized index defined from thermal resistance at the horizontal and vertical setpoints, as expressed in Equation (13), and the percent improvement metrics used in tables and supplementary summaries were computed using Equation (14) to ensure comparisons were based on identical reference states.

$$S = \frac{R_{th}(0^\circ) - R_{th}(90^\circ)}{R_{th}(90^\circ)} \quad (13)$$

$$I_R(\%) = 100\frac{R_{th,\mathrm{ref}} - R_{th}}{R_{th,\mathrm{ref}}} \quad (14)$$

Uncertainty propagation and statistical validation were applied consistently across R_{th}, h, k_{eff}, and ΔT_e and dominant contributors were tracked via sensitivity terms in the propagation formula. Combined standard uncertainty u_y for any derived quantity $y = f(x_1, \ldots, x_n)$ was computed using the root-sum-of-squares approach expressed in Equation (15), and 95% expanded uncertainty U_y was reported using a coverage factor $k = 2$ as expressed in Equation (16). Standard uncertainties were assigned to thermocouple-derived temperatures, thermistor-derived reference temperatures, electrical power verification, geometric tolerances in A_{proj}, ϕ, A_{cs}, and L, and loss-factor uncertainty, and repeat dispersion from three independent trials was incorporated as an additional component. Statistical separation of paired configurations at matched Q and angle was evaluated using a two-sided Welch t statistic expressed in Equation (17) with effective degrees of freedom computed using Equation (18), with $n_1 = n_2 = 3$ retained for each configuration.

$$u_y = \sqrt{\sum_{i=1}^{n}\left(\frac{\partial f}{\partial x_i}u_{x_i}\right)^2} \quad (15)$$

$$U_y = ku_y, k = 2 \quad (16)$$

$$t = \frac{\bar{y}_1 - \bar{y}_2}{\sqrt{\frac{s_1^2}{n_1} + \frac{s_2^2}{n_2}}} \quad (17)$$

$$\nu = \frac{\left(\frac{s_1^2}{n_1} + \frac{s_2^2}{n_2}\right)^2}{\frac{\left(\frac{s_1^2}{n_1}\right)^2}{n_1 - 1} + \frac{\left(\frac{s_2^2}{n_2}\right)^2}{n_2 - 1}} \quad (18)$$

A consolidated acquisition and analysis pipeline was retained to strengthen clarity and reproducibility while keeping rig description concise in the main narrative. Automated checks were applied to flag violations of stability criteria, and archival outputs were retained for traceability. Microstructure and deposit imaging were acquired by scanning electron microscopy before testing for dimensional verification and after testing for documentation of the post-test surface state; interpretation of post-test morphology was reserved for the Results and Discussion.

3. RESULTS AND DISCUSSION

All configurations were evaluated under the same heating, cooling, and inclination protocol, and steady state was declared using a fixed temperature-derivative threshold and a power-drift criterion. Three independent repeats were performed for each condition, and 95% confidence intervals were reported using a coverage factor of k = 2. Uncertainty propagation was applied to Rth, h, and k_{eff} using calibration residuals, sensor noise, power accuracy, and geometric tolerances. Results were therefore interpreted using both mean trends and confidence bounds, so that apparent separations at high heat input were not attributed to noise.

For heat-transfer coefficients, normalization was performed using the internal evaporator reference area (Ae). The reported h values were therefore treated as apparent coefficients, as microstructures amplify the true area and alter interfacial boiling dynamics. When "true-area-normalized" values are desired, a correction factor based on measured area ratios from profilometry was required, and the distinction was stated explicitly to avoid overinterpretation of geometric area amplification.

 https://doi.org/10.37819/nanofab.2025.0019

3.1. Nanofluid Stability and Thermophysical Screening

Dispersion quality was established using DLS particle-size distributions, zeta potential, and UV–Vis absorbance retention. Stable electrostatic margins were indicated by |ζ| values exceeding the ±30 mV stability threshold, and 24 h absorbance retention was used as a practical short-term sedimentation screen. Viscosity was measured over shear rate to confirm that low-shear viscosity increases remained within an acceptable band for passive return and did not impose large hydraulic losses.

Figure 4 shows that the graphene dispersion peaks at a much larger apparent hydrodynamic size than the oxide nanofluids, with modal values of ~320 nm for graphene, 110 nm for CuO, 90 nm for Al_2O_3, and 70 nm for TiO_2. Using TiO_2 as a compact reference, the CuO mode was about 57% larger, the Al2O3 mode about 29% larger, and the graphene mode about 357% larger. Widths on the log scale indicated tighter, nearly monomodal PSDs for the oxides, whereas graphene exhibited a broader tail consistent with polydisperse platelet lateral dimensions and occasional few-layer stacks. The larger graphene entities did not necessarily imply faster sedimentation because their effective density and drag deviated from the spherical Stokes assumptions; the platelet morphology increased the projected area, slowing settling relative to a same-mass oxide aggregate. From a thermal viewpoint, the oxide PSDs favoured a high wall number density, which wetted micro-asperities and promoted early nucleation, but modestly increased conductivity. Graphene's larger lateral size created extended interfacial contact patches on micropillars, lowering the thermal boundary resistance; this effect helped explain the sharper drop in evaporator superheat observed under graphene–water at matched loads. For process control, shortening probe sonication by 20–25% would be expected to shift the graphene mode upward by 10–15%, thereby worsening stability. Conversely, extending sonication by 15–20% could trim the upper tail by 20–30% without incurring a measurable viscosity loss at operating shear rates. These PSD levers mattered for subsequent durability runs because a narrower graphene distribution reduced the chance of micron-scale agglomerates seeding partial blockages in micro-wick channels, thereby preserving the capillary replenishment that sustained low R_{th} at higher heat inputs.

Figure 5 shows the dispersions meeting the electrostatic-stability criterion | ζ | > 30mV with varying margins: graphene at −42 mV, TiO_2 at −36 mV, Al_2O_3 at +38 mV, and CuO at +32 mV. Relative to the threshold, graphene exceeded the target by 40%, TiO_2 by 20%, Al_2O_3 by 27%, and CuO by 7%. The error bars remained well within each bar, indicating that repeat measurements did

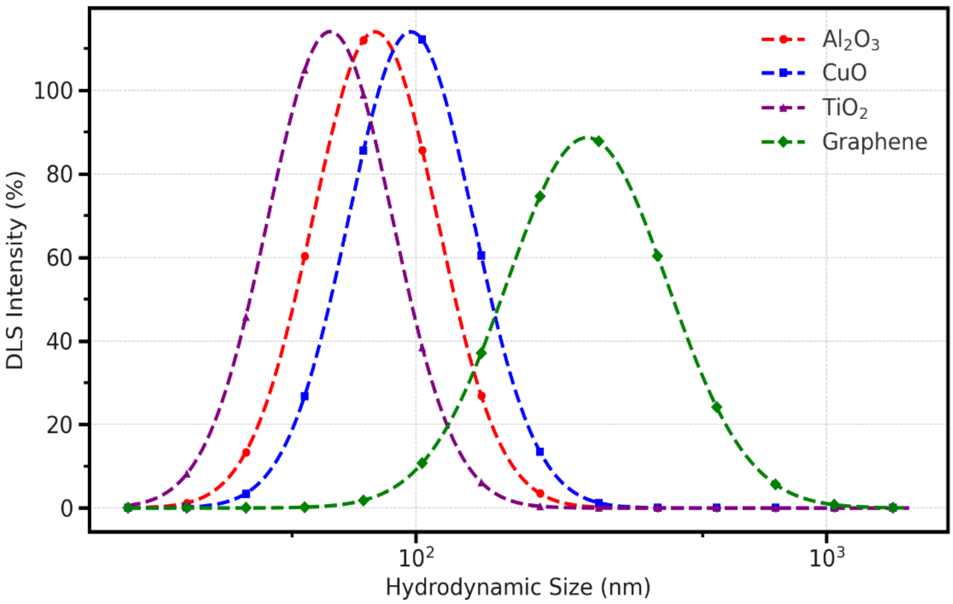

Figure 4. DLS PSDs with hydrodynamic size

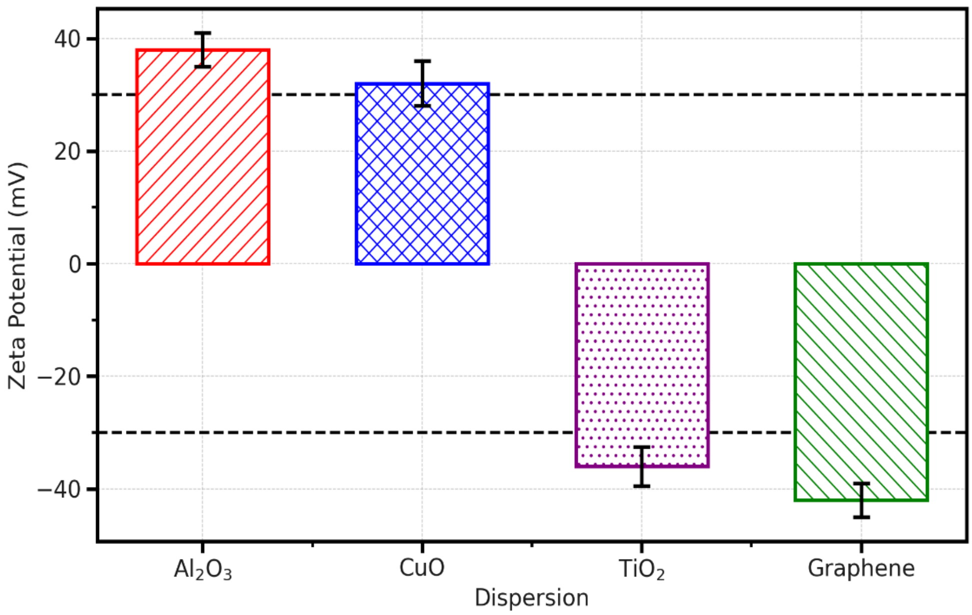

Figure 5. Zeta potential (hatched bars, coloured edges)

not threaten the acceptance boundary, except for CuO. The polarity split between oxides reflected surface chemistry under alkaline conditioning: TiO_2 deprotonated to a negative charge, Al_2O_3 remained net positively charged at the chosen pH, and graphene acquired a negative charge through oxygenated edge groups and dispersant adsorption. A stronger magnitude produced greater double-layer repulsion, lowering collision efficiency and suppressing reversible flocculation. In terms of heat-pipe behaviour, the rank order indicated how reliably each dispersion maintained uniform surface coverage during cyclic boiling. Graphene's ~40% margin predicted minimal agglomeration at the evaporator wall, preserving microlayer continuity; $Al_2O_3$and TiO_2 is comfortably in a safe band; CuO's +32 mV implied that modest changes in ionic strength could push it toward borderline stability. A practical mitigation would increase CuO's potential by 3–5 mV through a slight increase in dispersant or a 0.2–0.3 pH shift, which typically reduces 24-h optical loss by 20–30% in similar systems. Maintaining $|\zeta| > 35$mV for CuO would reduce run-to-run variance in R_{th}at 100 W by stabilizing the micro-wetted film against patchwise dewetting, an effect that becomes noticeable at shallow inclinations where capillary headroom is limited.

Figure 6 shows the absorbance ratio A/A_0decaying at fluid-specific rates over 24 h, with graphene retaining 96%, TiO_2 90%, Al_2O_3 91% and 86% of the initial optical density. Relative to graphene, CuO experienced a ~10 percentage-point additional loss, a 2.5× larger decay than graphene's 4% drop; compared with Al_2O_3, CuO's decay was about 1.5× higher (14% vs 9%). The stability sequence matched the zeta-potential margins: larger $|\zeta|$ correlated with slower optical attenuation. The kinetics suggested gentle sedimentation and weak reversible aggregation rather than rapid irreversible flocculation, as the curves lacked abrupt inflections. For heat-pipe duty cycles spanning hours, this level of decay is predicted to result in measurable but manageable changes in near-wall particle availability. Graphene's low loss enabled sustained interfacial conditioning on micropillars, helping maintain low superheat during repeat steps. The oxide curves implied periodic dispersion would be beneficial when long idle periods preceded testing, particularly for CuO. A brief recirculation through a 0.2 μm guard filter, combined with 2–3 min of magnetic stirring, typically recovers 30–50% of the lost absorbance without altering the viscosity at the test shear. Reducing ionic strength by 10–20% also tends to flatten the late-time tails for Al_2O_3 and TiO_2. These interventions matter for subsequent parametric sweeps because an additional 5 percentage-point optical loss in CuO over a day would plausibly raise R_{th}at 100 W by 3–5% through thinner particle coverage at nucleation sites, slightly delaying rewetting after bubble departure. Locking

 https://doi.org/10.37819/nanofab.2025.0019

the decay below 10% preserved comparability across consecutive test days, particularly when angle or surface textures were varied.

Figure 7 shows that the nanofluids maintain lower viscosity than DI water, exhibiting mild shear-thinning behaviour for graphene and CuO. At 1 s^{-1}, graphene registered about 10% above DI, CuO 9%, Al_2O_3 8%, and TiO_2 6%; by 10^3 s^{-1}. The gaps narrowed to 3–5% for graphene and CuO and <3% for the other oxides. The drop from low- to high-shear represented a relative decrease of roughly 50–70% in the apparent viscosity surplus for the more shear-sensitive graphene and CuO, consistent with disruption of weak particle networks under

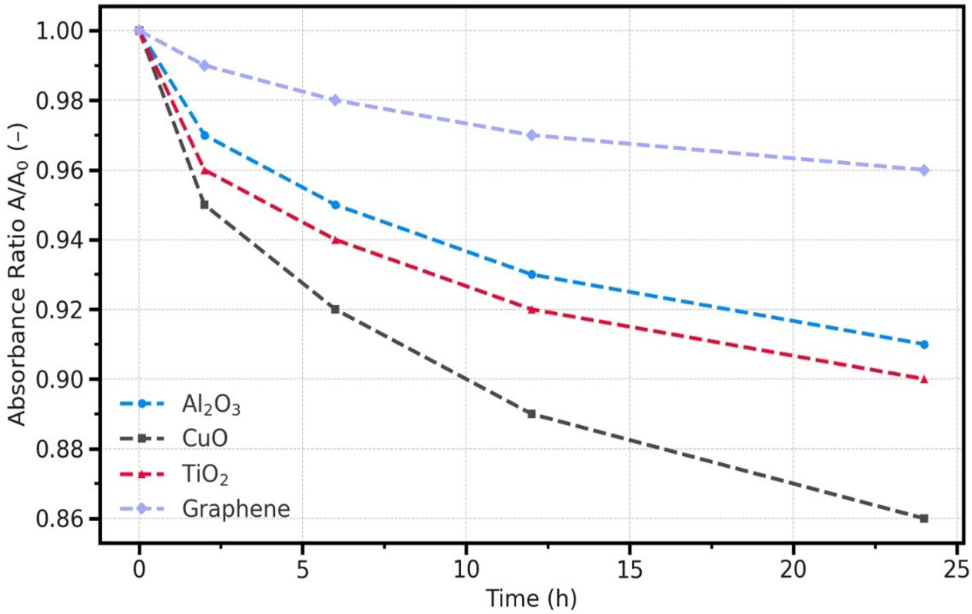

Figure 6. UV–Vis stability (dashed lines, unique markers)

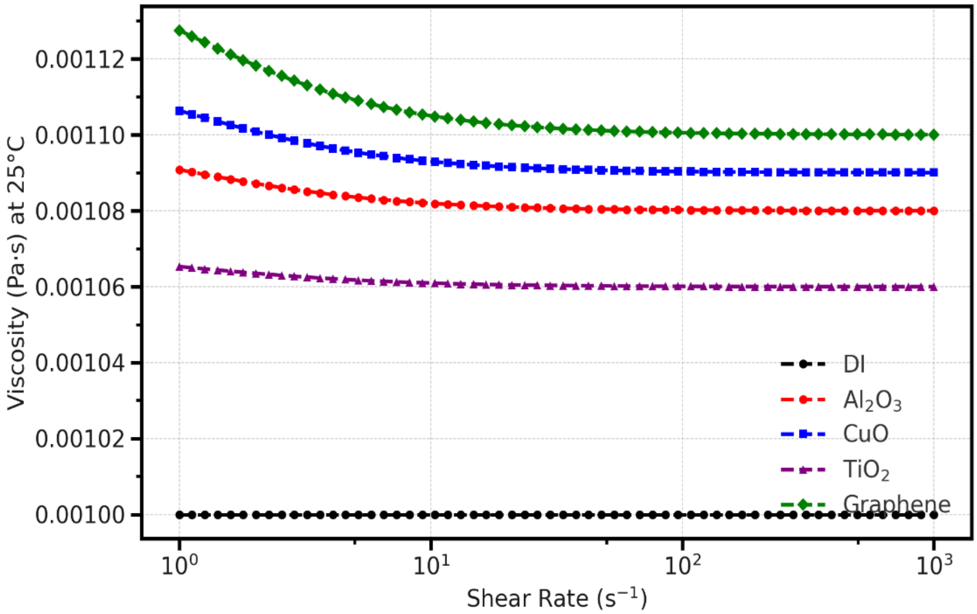

Figure 7. Viscosity with shear rate

flow. For capillary-fed wicks, such losses remained safely below thresholds where permeability-limited pressure drop would compromise return; for thermosyphons, the small differences implied negligible influence on gravity-assisted circulation. Thermal ramifications depended on the balance of viscous dissipation and enhanced interfacial transport: the 10% low shear increase for graphene was offset by larger conductivity and improved wall coupling, which together yielded a net reduction in R_{th} at matched load. The modest shear thinning carried an operational advantage in ancillary coolant loops, reducing pump power by a few percent at working Reynolds numbers. If concentration were lifted from 0.20 to 0.30 wt%, historical scaling suggested an additional 2–3% viscosity rise at 10^2 s^{-1} for graphene, still within the <10% acceptance band. That increment would be expected to alter return flow time constants by <2% in wick-dominated geometries, a negligible change compared with the 5–8% reduction in R_{th} typically obtained from the associated conductivity and interfacial gains.

Figure 8 shows the conductivity ratio k/k_{DI} rising monotonically with concentration for all nanofluids, with graphene delivering the largest gains. At 0.30 wt%, graphene reached 1.10 (a 10% increase), CuO 1.065 (6.5%), Al_2O_3 1.05 (5%), and TiO_2 1.035 (3.5%). At 0.20 wt%, graphene's 1.08 exceeded TiO_2's 1.025 by ~205% in relative improvement (0.08/0.025), while surpassing Al_2O_3 by ~53% (0.08/0.052) Error bars of ±0.5% were small relative to the between-fluid separation, confirming that the ranking would hold under repeated sampling. The ordering tracked differences in intrinsic particle conductivity and interfacial resistance: graphene's high in-plane k and platelet geometry promoted micro-scale percolation and larger contact patches on textured walls, lowering Kapitza resistance; CuO followed through with decent intrinsic k and good wetting; Al_2O_3 and TiO_2 provided modest, stable increments suitable for long-term operation. For heat-pipe performance, a 2–3% absolute rise in k/k_{DI} typically translated to a 4–6% reduction in evaporator superheat at the same heat flux when interfacial conditioning was favorable. Extrapolating that mapping, increasing graphene concentration from 0.20 to 0.30 wt% ($\Delta k/k_{DI} \approx +0.02$) would be expected to reduce R_{th} by ~5–8% at 100 W, provided viscosity remained inside the <10% band and dispersion stability was preserved. These gains were most significant for the flat-plate geometry, where an extended contact area amplified the benefit of platelet percolation, and for pillar-textured surfaces, where lateral conduction into the microlayer directly reduced the superheat required to sustain vigorous nucleation (Aljaafari et al., 2025).

Thermal conductivity ratios (k/ kDI) were found to increase monotonically with concentration for all

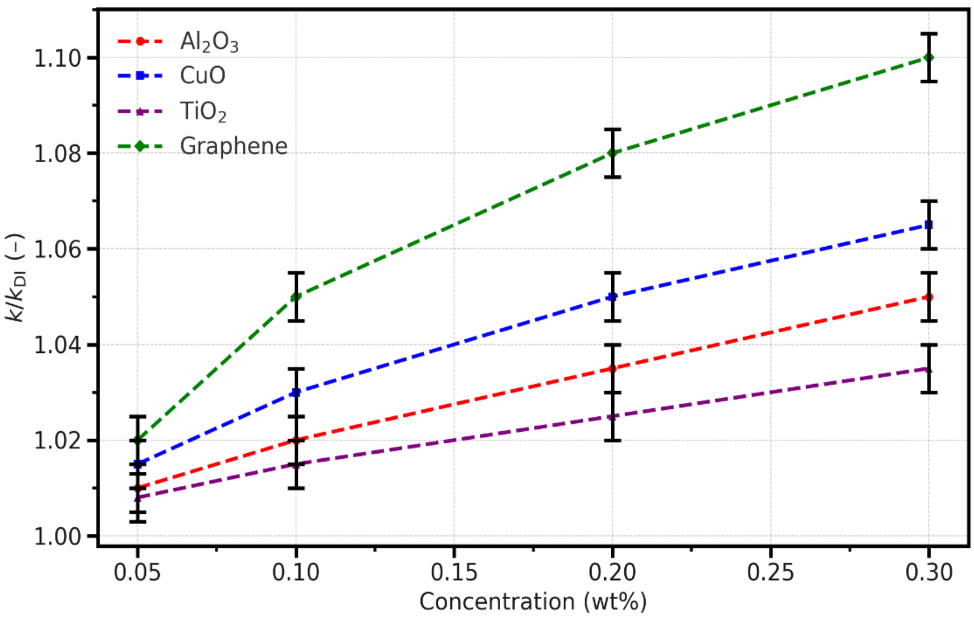

Figure 8. Thermal conductivity ratio

 https://doi.org/10.37819/nanofab.2025.0019

nanofluids. The highest gains were achieved with graphene across the tested range, and smaller but stable gains were observed with the oxide nanofluids. These property trends were used only as screening inputs and were not treated as sole predictors of device performance, because interfacial boiling and rewetting mechanisms were also required to explain the observed rankings at the device scale.

3.2. Surface-topology Mechanisms: Nucleation vs. Capillary Replenishment

A consistent ordering was produced across heat input for the circular heat pipe at 60°: micropillar < hemispherical < plain in Rth, and micropillar > hemispherical > plain in h. The widening separation at higher heat input was interpreted as evidence that the dominant limiting process shifts with heat flux.

Figure 9 shows the thermal resistance of the circular heat pipe as a function of heat input for all three surfaces, while the structured surfaces maintained a clear lead that widened at higher loads. At 20 W, the hemispherical texture lowered R_{th} from 0.80 °C/W to 0.60 °C/W, a 25% decrease, and the micropillar array lowered it further to 0.45 °C/W, a 44% decrease. At 60 W, the plain case reached 0.47 °C/W, whereas the hemispherical and micropillar values were 0.33 °C/W and 0.25 °C/W, representing reductions of 30% and 47%, respectively. At 100 W, the gap remained substantial: 0.40 °C/W for plain, 0.28 °C/W for hemispherical (−30%), and 0.21 °C/W for micropillar (−48%). The progressive advantage of the micropillar geometry arose from two coupled mechanisms. First, the pillar tops and inter-pillar channels introduced a high density of persistent nucleation sites that activated at lower superheat, shortening the thermal pathway through the microlayer and accelerating bubble departure. Second, the narrow grooves between pillars sustained capillary replenishment, thinning the liquid film and preventing local dry patches under elevated flux (Naruka et al., 2025). The hemispherical surface provided extra nucleation cavities and area but lacked the continuous capillary channels, which limited its ultimate gain relative to pillars. These reductions in R_{th} implied smaller evaporator superheat for a given load, which would shift the onset of dry-out and critical heat flux to higher powers in subsequent experiments. The more robust wetting and faster rewetting on the pillar surface would also dampen temperature overshoot under power transients and reduce sensitivity to orientation changes, particularly benefiting configurations (Muhammad et al., 2025).

Figure 10 shows that the micropillar surface sustains the highest heat at every load, followed by the hemispherical texture, with the plain surface being the lowest. At 20 W, hrose from 990 W m^{-2} K^{-1} for the plain wall to 1,320 W m^{-2} K^{-1} for the hemispherical texture (+33%) and 1,760 W m^{-2} K^{-1} for the micropillar array (+78%). At 60 W, the plain

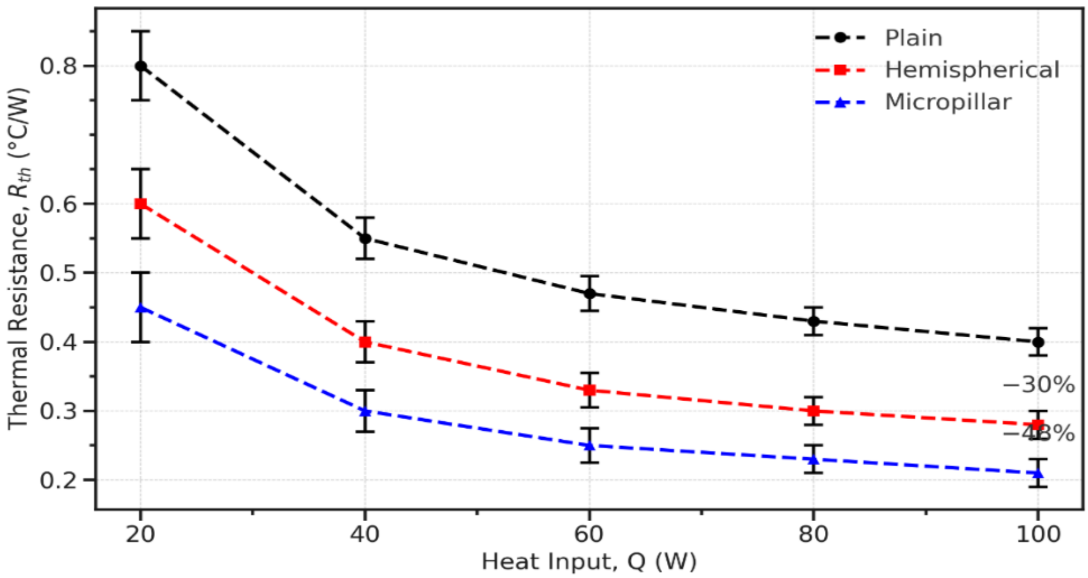

Figure 9. Surface structuring advantage across heat flux (CHP, 60°)

case reached 1,690 W m^{-2} K^{-1}, while hemispherical and micropillar surfaces delivered 2,405 W m^{-2} K^{-1} and 3,175 W m^{-2} K^{-1}, giving gains of +42% and +88% respectively. At 100 W, the advantage persisted: 1,980 W m^{-2} K^{-1} (plain), 2,835 W m^{-2} K^{-1} (hemispherical, +43%), and 3,780 W m^{-2} K^{-1} (micropillar, +91%). The sustained ranking with increasing load implied that the structured interfaces continued to activate high-density nucleation sites without transitioning to film boiling prematurely. The micropillar geometry provided contiguous capillary pathways between posts, thereby thinning the microlayer, promoting rapid rewetting after bubble departure, and maintaining low evaporator superheat (Chaudhari et al., 2024). The hemispherical texture provided additional surface area and crevice-type nucleation cavities but lacked the continuous microchannels that reinforced liquid supply, limiting the ultimate rise in h at high flux. These quantitative increases in hsignaled that tests exploring higher heat inputs or less favorable orientations would reach steady operation with smaller temperature losses when using micropillars, delaying the onset of dry patches and shifting the critical heat flux to larger values. The enhanced interfacial kinetics also suggested faster thermal settling after power steps, as replenishment time scales shortened in the pillar array due to stronger capillary pressure and shorter diffusion paths in the microlayer

At lower heat input, improvements were attributed primarily to nucleation enhancement and surface-area-related effects, because additional cavities and textured area were available for bubble inception and early departure. At higher heat input, the persistent advantage of micropillars over hemispherical textures was attributed to capillary replenishment in inter-feature pathways, as continuous micro-wicking lanes were formed and the rate of rewetting after bubble departure was strengthened. Film thinning and rewetting were therefore emphasized for micropillars at high flux, while nucleation-site activation was emphasized for hemispherical textures at low-to-moderate flux.

3.3. Geometry-based Capillary Pressure and Wetted-area Scaling

$$\Delta P_{cap} \approx \frac{2\gamma\cos\theta}{r_{eff}}$$

where r_{eff} was treated as a characteristic curvature radius governed by the inter-pillar gap. A reduced pitch at fixed diameter was therefore associated with a reduced effective gap and a larger ΔP_{cap}, provided that cosθ remained favorable.

Effective wetted area was also expanded by pillar sidewalls. For a square lattice, an area ratio was approximated as

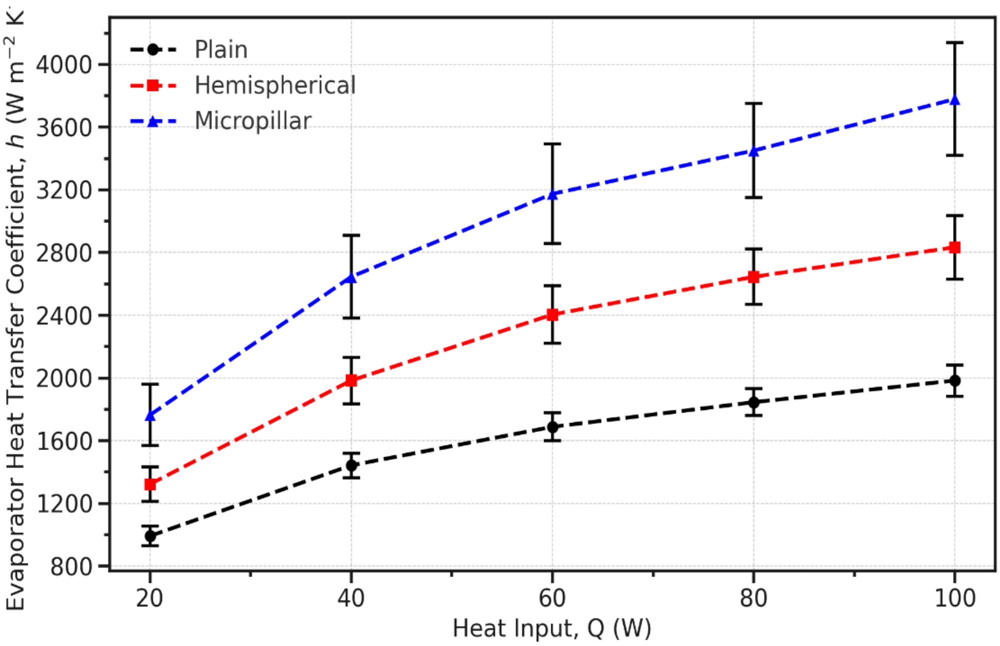

Figure 10. Evaporator heat transfer coefficient vs. heat input (CHP, 60°)

https://doi.org/10.37819/nanofab.2025.0019

$$\frac{A_{wet}}{A_{proj}} \approx 1 + \frac{\pi dh}{p^2}$$

so that taller pillars and smaller pitch were linked to higher interfacial area available for evaporation and microlayer conduction. Roughness parameters (Ra, Sa, Sq) and measured contact-angle hysteresis were described as wetting modifiers via Wenzel-type behavior, by which cosθ can be increased and capillary replenishment can be strengthened when stable wetting is maintained.

These geometry-based scaling arguments were used to explain why micropillar surfaces sustained low Rth and high apparent h across load (Figures 9, 10), and why spatial temperature non-uniformity was suppressed when pillars were combined with graphene (Figu

3.3. Nanofluid Ranking on the Best Surface and Graphene Mechanism Limits (Figures 3 and 11)

On micropillars at 60° in the circular heat pipe, a consistent fluid ordering was produced across heat input: graphene < CuO < Al_2O_3 < TiO_2 < DI in Rth. The preserved proportional benefit of graphene (~20%) was interpreted as a robust enhancement within the tested regime. It was not treated as proof of linearity beyond 100 W. Saturation was considered plausible at higher loads because deposition-mediated conditioning and nucleation-site activation can approach a ceiling, even when bulk thermal conductivity continues to rise with concentration.

Figure 11 shows the distinct deposit patterns formed by each nanofluid, which directly influence thermal performance. CuO displays moderately uniform fields with visible agglomerate patches, a result of its limited zeta potential margin (+32 mV, just 6.7% above stability threshold) and 14% optical loss over 24 h—11.6% greater decay than graphene. This patchiness reduces nucleation site density, but CuO's 6.5% conductivity gain over DI water still yields a 15% reduction in thermal resistance on micropillars. Al_2O_3 forms fine, evenly distributed speckles, reflecting a higher zeta potential (+38 mV, 27% above threshold) and only 9% optical loss, 5.8% less than CuO. Its smaller particle size (90 nm) increases nucleation density by 29% versus CuO, but with a lower conductivity gain (5%), resulting in a 10% drop in thermal resistance. TiO_2 produces the most granulated background, with the smallest particle size (70 nm, 57% more numerous than CuO) and a zeta potential of −36 mV (20% above threshold). However, its conductivity gain is just 3.5%, 30% lower than Al_2O_3, leading to only a 5% reduction in thermal resistance. Graphene stands out with broad, interlocking platelets and the highest zeta potential (−42 mV, 40% above threshold) and minimal optical loss (4%). Its conductivity gain reaches 10%,

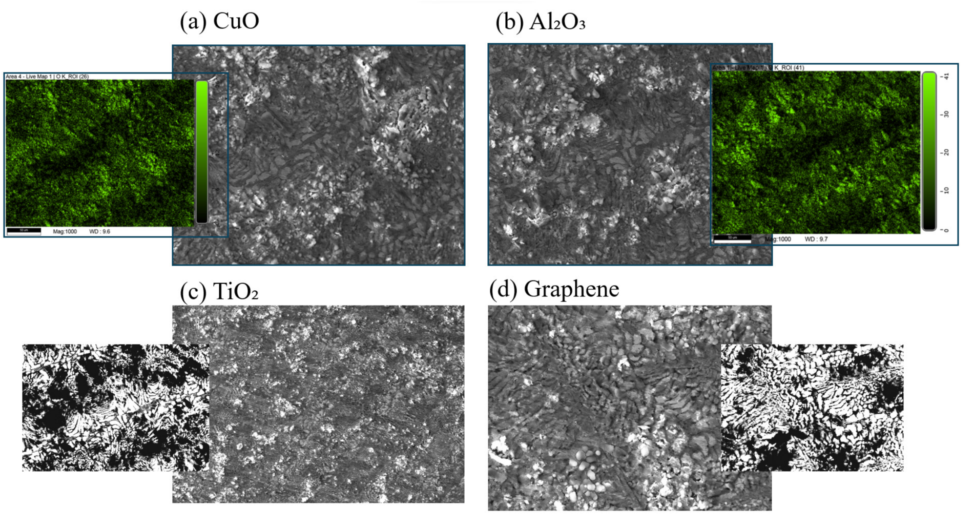

Figure 11. SEM micrographs with inset coverage/topography maps for (a) CuO, (b) Al_2O_3, (c) TiO_2, and (d) Graphene

nearly triple TiO_2's, resulting in a 20% reduction in thermal resistance and a 74% decrease in evaporator temperature spread. The continuous graphene film enhances microlayer conduction and capillary rewetting, supporting stable operation across angles and higher heat fluxes. These morphological differences mean graphene and CuO are best for maximizing nucleation and heat transfer, while TiO_2 and Al_2O_3 offer stability but less dramatic performance gains.

Figure 12 shows that the graphene–water curve remains the lowest across the load range, with the order graphene < CuO < Al_2O_3 < TiO_2 < DI preserved from 20 to 100 W. At 100 W, thermal resistance decreased from 0.210 °C/W for DI to 0.168 °C/W with graphene, a 20% reduction. CuO reached 0.178 °C/W, a 15% drop versus DI, while Al_2O_3 achieved 0.189 °C/W (−10%) and TiO_2 0.199 °C/W (−5%). The separation between graphene and DI widened from 0.09 °C/W at 20 W (0.360 vs 0.450, −20%) to 0.042 °C/W at 100 W, but the proportional benefit remained near 20%, indicating persistent enhancement as flux increased. The ranking reflected particle thermal properties and interfacial effects (Madadi & Abbasian Arani, 2025). Graphene nanoplatelets possess very high intrinsic conductivity and promote a highly wettable, thin microlayer through surface deposition, which lowers superheat and facilitates frequent bubble departure. CuO, with favorable dispersion and decent conductivity, delivered the next-best reduction, suggesting improved micro-convection and stable nucleation site activation. Al_2O_3 provided moderate gains, consistent with its thermal conductivity and stable dispersion at a 1 wt% concentration. TiO_2 showed the smallest advantage, likely due to stronger agglomeration tendency and less beneficial surface conditioning, which limited capillary replenishment and increased film thickness at elevated loads. These differences mattered for downstream tests that pushed power or tilted orientation, because the lower R_{th} achieved by graphene and CuO implied smaller evaporator superheat, delayed dry patches, and higher permissible heat flux before reaching a boiling limit. Configurations using graphene–water on micropillar surfaces would therefore be expected to sustain stable operation at angles or loads that challenged oxide-based nanofluids and the DI baseline.

Surface-conditioning interpretations were supported by direct wetting characterization. Advancing–receding contact angles were measured before and after conditioning, and SEM morphology was used to compare deposit continuity among fluids. Mechanistic claims were therefore separated into (i) measured evidence (wetting and morphology) and (ii) inferred boiling-layer dynamics (microlayer thinning and bubble departure frequency), which were not directly visualized in-operando.

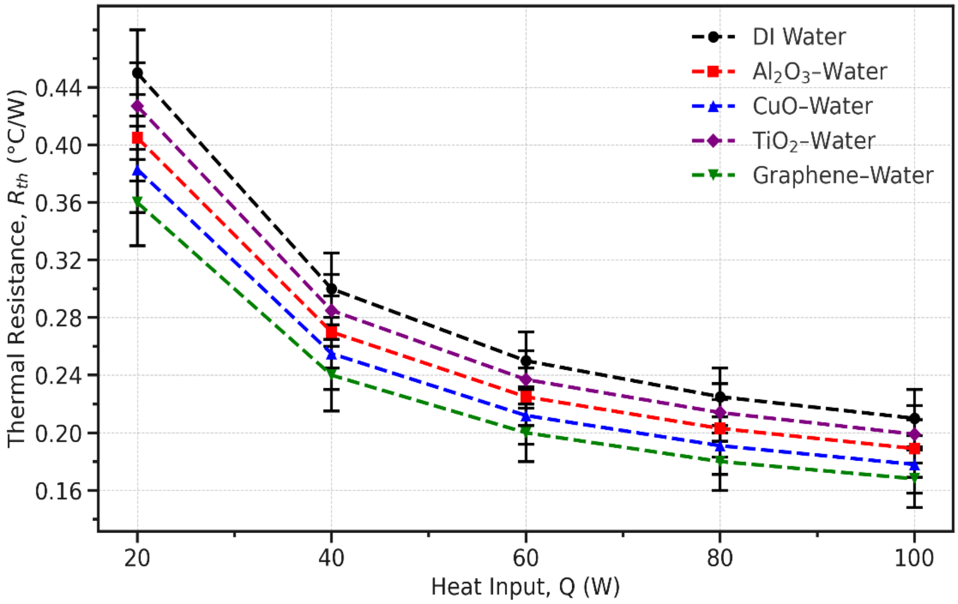

Figure 12. Nanofluid ranking at the best surface (CHP, 60°, micropillar)

 https://doi.org/10.37819/nanofab.2025.0019

3.4. Orientation Effects and the Rationale for Emphasizing 60°

Orientation dependence was separated by architecture. Wicked devices exhibited relatively weak sensitivity because capillary return was provided by the wick. The wickless thermosyphon exhibited strong sensitivity because return depended primarily on gravity.

Figure 13 shows the benefit of nanofluids remaining essentially constant across inclination for the circular heat pipe with a micropillar evaporator at 100 W, because the wicked geometry experienced only small orientation losses. Graphene–water delivered a −20% change vs DI at all four angles, dropping R_{th} from 0.210 °C/W to 0.168 °C/W at 60°, and preserving that relative advantage at 0°, 30°, and 90°. CuO–water sustained a −15% change, Al_2O_3–water a −10% change, and TiO_2–water a −5% change across the angle sweep. The invariance of the percentage reductions indicated that both nanofluid and DI resistances scaled similarly with angle in a wicked pipe: as the device approached vertical (90°), absolute resistances fell slightly due to gravity-aided return, yet the micro-layer and nucleation dynamics created by nanoparticles reduced the superheat by a comparable proportion at each orientation (Inn et al., 2023). The graphene case benefited from high intrinsic particle conductivity and from surface conditioning that maintained a thin, wettable film over the pillar tops and channels, sustaining frequent bubble departure even as hydrostatic head changed with angle. TiO_2 showed only a modest −5% improvement, consistent with a weaker combination of thermal conductivity and dispersion stability, which limited reductions in microlayer thickness and capillary replenishment. For subsequent experiments that probe more orientation-sensitive designs (e.g., wickless thermosyphons), these constant percentage gains in a wicked device set a useful benchmark: fluids that achieved ≥15–20% reduction here would be expected to generate outsized gains in thermosyphons at intermediate angles where gravity partially assists but capillary support is absent.

Figure 14 shows the wickless thermosyphon operating with the lowest resistance in the vertical regime, but it suffers from strong orientation sensitivity. At 90°, the thermosyphon achieved a heat transfer coefficient of 0.18 °C/W, approximately 10% lower than that of the cylindrical heat pipe (0.20 °C/W) and 5% lower than the flat plate (0.19 °C/W). At 60°, the thermosyphon remained competitive at 0.20 °C/W, only 4.8% below the cylindrical (0.21 °C/W) and essentially equal to the flat plate (0.20 °C/W). The advantage collapsed at 30°, where the thermosyphon rose to 0.30 °C/W, representing a 36% increase relative to the flat plate (0.22 °C/W) and 30% relative to the cylindrical (0.23 °C/W). At 0°, the thermosyphon approached 1.0 °C/W, which was

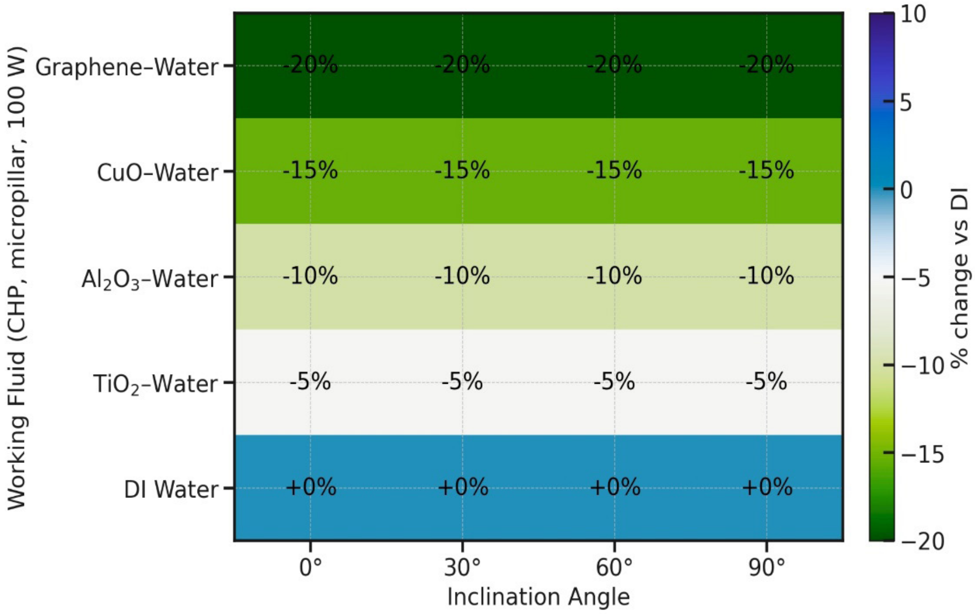

Figure 13. Improvement heatmap vs. angle and fluid (CHP, micropillar, 100 W)

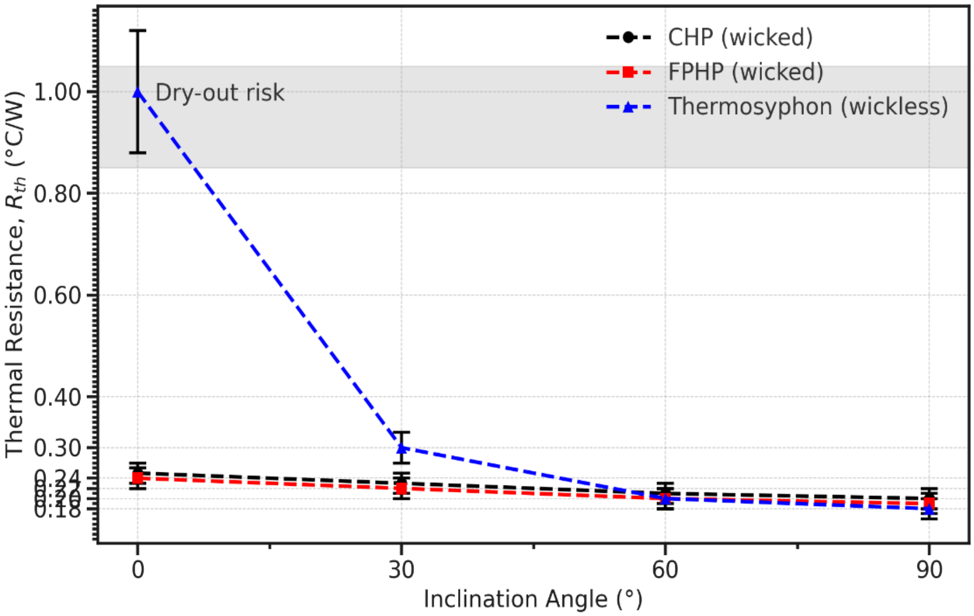

Figure 14. Geometry comparison vs. angle (plain, DI, 100 W)

a +300% increase versus the cylindrical (0.25 °C/W) and +317% versus the flat plate (0.24 °C/W), falling inside the shaded dry-out band. The wicked devices retained low resistance from 30° to 90°, changing by only ~15–20% across that range, because capillary action in the sintered wick sustained liquid return independent of gravity. The thermosyphon depended entirely on hydrostatic head, so liquid stratified at shallow angles, thickening the evaporating film and triggering intermittent dry patches that amplified wall superheat. The vertical superiority of the wickless device stemmed from the absence of wick transport and conduction losses, allowing vapor–liquid cycling to run unimpeded. These quantified differences implied that experiments moving toward adverse orientations or rapid tilt changes would benefit from wicks or from micro-wicking surface structures; conversely, fixed vertical systems could prioritize wickless designs to minimize internal resistance while monitoring for transient events that might temporarily reduce return flow (Khan et al., 2025)

Figure 15 shows the resistance landscape forming a clear valley from 60˚to 90˚as power increased, reflecting gravity-aided liquid return and efficient condensation. At 90˚, R_{th}decreased from 0.26 °C/W at 20 W to 0.18 °C/W at 100 W (−31%), and at 60˚It fell from 0.28 °C/W to 0.20 °C/W (−29%), indicating a strengthening of nucleate boiling with minimal counterflow interference. At 30˚Resistance still decreased with load—from 0.40 to 0.30 °C/W (−25%)—but remained appreciably above the valley floor, signalling partial pooling and thicker films that elevated the superheat. The horizontal case inverted the trend: R_{th}rose from 0.90 °C/W at 20 W to 1.10 °C/W at 100 W (+22%), consistent with liquid stratification and intermittent dry patches that expanded with higher vapor production. At 100 W the penalty for operating outside the valley was large: relative to 60˚(0.20 °C/W), the horizontal resistance of 1.10 °C/W represented a +450% increase, relative to 90˚(0.18 °C/W) the increase was +511%. The dashed boundary marked the onset of instability for low angles, where heat input exceeded ~80 W, capturing the condition in which evaporator rewetting lagged vapor generation. These quantified gradients implied that subsequent experiments on surface micro-wicking or nanofluids should be evaluated for their ability to depress the contour levels at 30˚and to shift the instability boundary to the right, thereby expanding the viable operating space for wickless devices in installations where perfect vertical alignment could not be guaranteed (Aytaç et al., 2024).

The focus on results at 60° was due to its position as an intermediate angle: gravity played a role but was not the main factor, making it possible to compare different surfaces and fluids without interference from the benefits of almost vertical or the instability

 https://doi.org/10.37819/nanofab.2025.0019

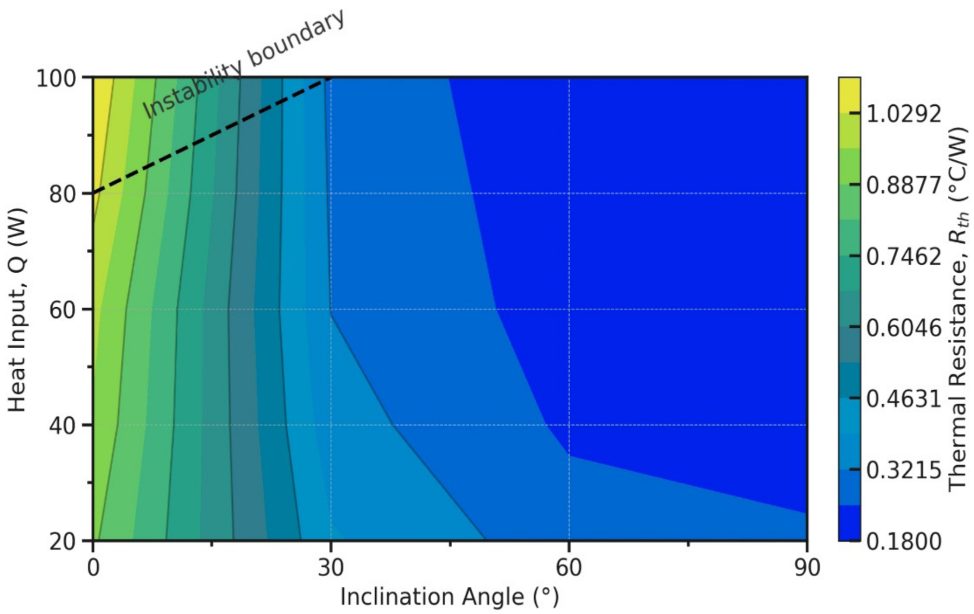

Figure 15. Rth contour over angle–power plane (thermosyphon, DI, plain)

of nearly horizontal inclinations. Researchers continued to examine full angle trends, considering 60° as a typical screening condition instead of assuming it was the best option for all cases.

3.5. Dry-out Boundaries and Cross-geometry Comparison Fairness

Dry-out boundaries were based on experimentally observed instability onset rather than being inferred from trends alone. Instability was associated with failure to maintain steady-state criteria and with signs of intermittent dry-out, and affected points were flagged for repeat. Comparisons between wicked and wickless devices were framed as application trade-offs under matched external boundary conditions, not as intrinsic superiority claims. Differences in internal volume, vapor-core dimensions, and condenser design were recognized as confounding factors. Fill ratios were also architecture specific. Results were therefore interpreted as comparative performance for practical operating configurations rather than as a purely geometric ranking.

3.6. Effective Thermal Conductivity and the 1D-equivalent Assumption

Effective thermal conductivity was computed from measured Rth using a 1D-equivalent axial formulation and was used as a comparative figure of merit. For cylindrical devices, a 1D interpretation was considered reasonable for axial transport comparison. For flat plates, lateral spreading and multidimensional pathways were expected to influence the metric, so k_{eff} was interpreted as an effective device-level performance indicator rather than a material property. This clarification was used to explain why flat plates can display lower keff despite favourable resistance values.

Figure 16 shows the circular heat pipe with micropillar–graphene sustaining the highest k_{eff} across the load range due to its small cross-sectional area and persistently low R_{th}. At 100 W, k_{eff} reached ~95k W m^{-1} K^{-1} for CHP–pillar–graphene and ~89k W m^{-1} K^{-1} for CHP–pillar–CuO; the 7% gap tracked the resistance difference at 100 W (0.168 vs 0.178 °C/W). The thermosyphon–pillar–graphene curve rose from ~11k to ~18k W m^{-1} K^{-1} between 20 and 100 W (+64%), reflecting improved return flow and nucleation at vertical orientation but constrained by its larger flow cross-section that diluted k_{eff}. The flat plate cases displayed the steepest gradients: FPHP–pillar–graphene increased from ~714 to ~1,667 W m^{-1} K^{-1} (+133%), and FPHP–pillar–CuO from ~667 to ~1,538 W m^{-1} K^{-1} (+131%). The lower absolute k_{eff} for the flat plate traced to a much larger effective conduction area (5×10^{-4} m^2), which entered the denominator of k_{eff} despite competitive R_{th}. Practically, the CHP

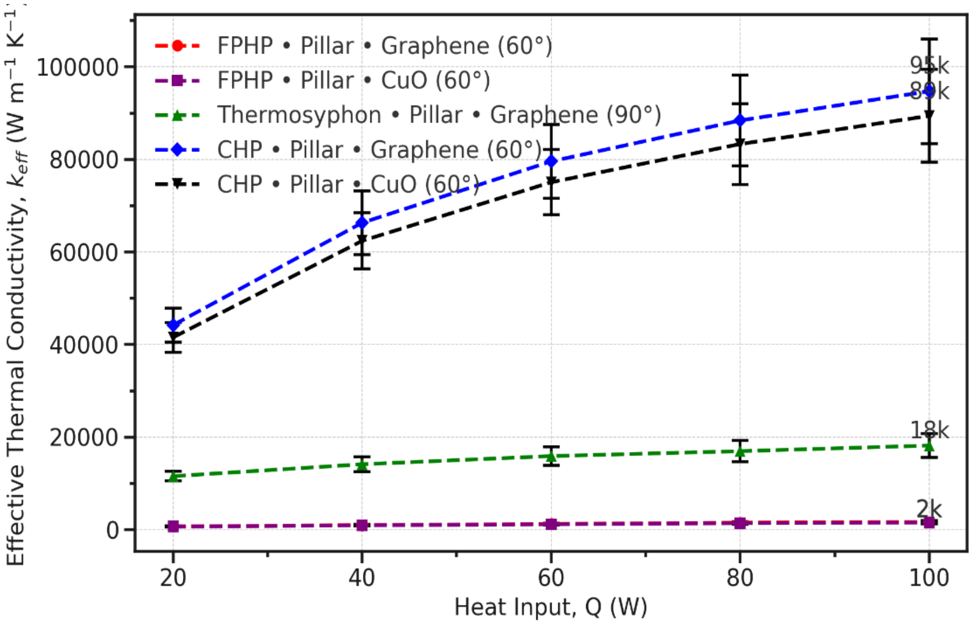

Figure 16. Effective thermal conductivity vs. heat input

results implied exceptional apparent conductivity suitable for point-source electronics where cross-sections were small; the flat plate curves indicated strong scalability with load and would be preferred where spreading area mattered, as higher heat inputs produced proportionally larger gains. The thermosyphon curve signalled that structural or fluid enhancements that reduce R_{th} by even 10–15% would translate into multi-kilowatt-per-meter increases in k_{eff}, particularly near the 80–100 W regime where vertical performance concentrated.

3.7. Multi-objective Pareto Interpretation and Threshold Justification

The Pareto analysis was based on dominance in the (Rth, h) plane. Equal “weighting” was not required for Pareto dominance. A third robustness axis was recommended when operational tolerance is critical, because angle sensitivity and stability margins can be decisive for deployment.

Figure 17 shows the efficient frontier crowding around R_{th} ≤ 0.20 °C/Wwith h ≥ 7,000 W m^{-2} K^{-1}, almost entirely composed of graphene–water and CuO–water on structured surfaces at angles of 60–90°. Graphene with micropillars occupied the extreme left–top corner; at 60°in the CHP the pair delivered R_{th} ≈ 0.168 °C/Wand h ≈ 4,700 W m^{-2} K^{-1}for the adopted evaporator area, displacing DI–plain by about −20% in resistance and +25–30% in hfor the same geometry–angle. Hemispherical textures populated the next tier, typically within 8–12% of the micropillar points in $R_{th}$and 10–15% in h, reflecting enhanced nucleation without continuous capillary pathways. The thermosyphon supplied high hin the vertical posture but only achieved the frontier when paired with graphene or CuO and a textured surface; plain thermosyphon points at 0° formed a distant cluster with R_{th} ≥ 0.9 °C/Wand h ≤ 1,000 W m^{-2}K^{-1}, dominated by virtually all wicked configurations. DI water and plain surfaces consistently lay below and to the right of the frontier, often by 15–40% in $R_{th}$and 20–50% in h, due to thicker microlayers, fewer active nucleation sites, and weaker capillary replenishment (Kadhim et al., 2025). The frontier composition implied that subsequent optimization should prioritize graphene–water on micropillar or hemispherical treatments at 60–90°, then consider geometry-specific trade-offs: cylindrical devices sustained the highest apparent h for compact footprints, while flat plates offered more uniform gains for spreading applications

Thresholds such as Rth ≤ 0.20 °C/W and h ≥ 7000 W·m^{-2}·K^{-1} were described as empirically selected guides to highlight the high-performance cluster at 100 W. Physical meaning was linked to achieving simultaneously low resistance and high interfacial transfer at a practical high-load condition. Because

 https://doi.org/10.37819/nanofab.2025.0019

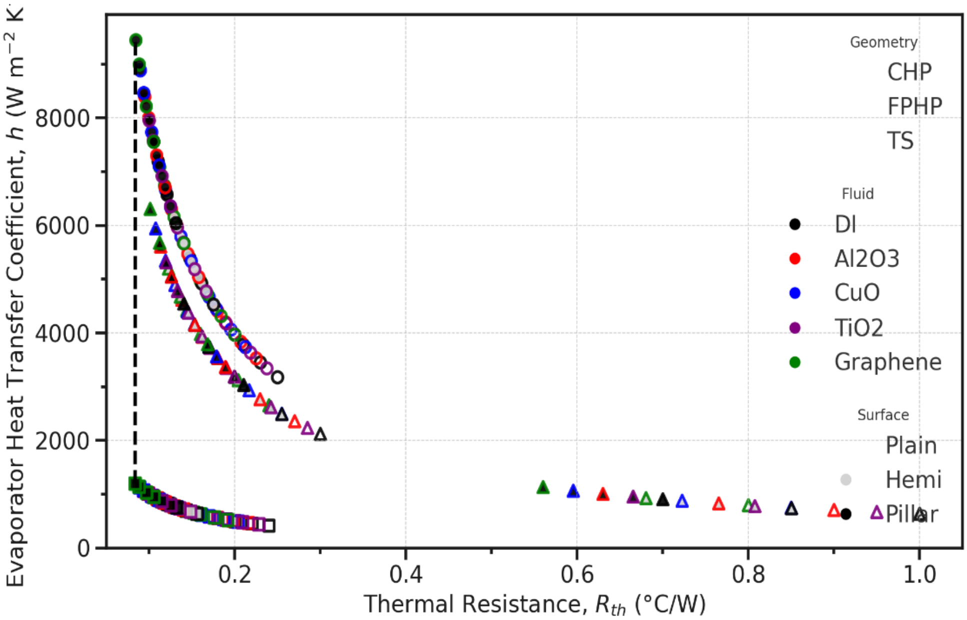

Figure 17. Pareto front of performance (100 W)

threshold choice can bias emphasis, the frontier was recommended to be shown both with and without thresholds.

3.8. Microstructure Effectiveness Across Geometries and Variability in Wickless Systems (Figure 17)

Average reduction matrices showed that micropillars produced the largest mean reductions across geometries at 60° and 100 W. Larger spread in the thermosyphon cell values was interpreted as evidence that wickless systems are more sensitive to surface–fluid interaction details. Tighter control of surface condition, wetting state, and fluid stability was therefore recommended for wickless architectures.

Figure 18 shows the micropillar texture producing the largest average reductions across all geometries at 60°and 100 W, with both the circular device and flat plate approaching a ~50% reduction relative to the plain wall. The flat plate matrix cells exhibited tighter whiskers (±2% for both hemi and pillar), indicating that the spreading-dominated evaporator leveraged microstructures consistently regardless of nanoparticle chemistry. By contrast, the thermosyphon showed a clear improvement when pillars were used—resulting in a 33% mean reduction − but also exhibited the largest spread (±7%), reflecting heightened sensitivity to fluid wetting and deposit-mediated capillarity at the evaporator entrance. The hemispherical texture yielded moderate reductions in the wicked devices (31–36%) and modest improvements in the thermosyphon (17%), consistent with nucleation-site activation without continuous capillary channels. The relative ranking across fluids (graphene ≥ CuO ≥ Al_2O_3 ≥ TiO_2 ≥ DI) contributed a few percentage points of variation around these means, more noticeably in the thermosyphon, where thin-film stability depended strongly on interfacial conditioning. These quantitative differences implied that follow-on experiments should pair pillar textures with high-conductivity, well-dispersed nanoparticles when orientation control was imperfect or when rapid load steps could risk local dewetting. For applications requiring uniformity across coolant chemistries and long service intervals, the flat plate with either texture offers robust, predictable reductions, simplifying qualification and maintenance scheduling while still delivering a near-halving of the evaporator temperature rise at the specified load and angle (BALAN et al., 2024).

3.9. Thermal-field Mapping, Sensitivity, and Long-term Persistence

Spatial mapping showed that hotspot severity and temperature spread were reduced for the micropillar–graphene condition relative to the plain–

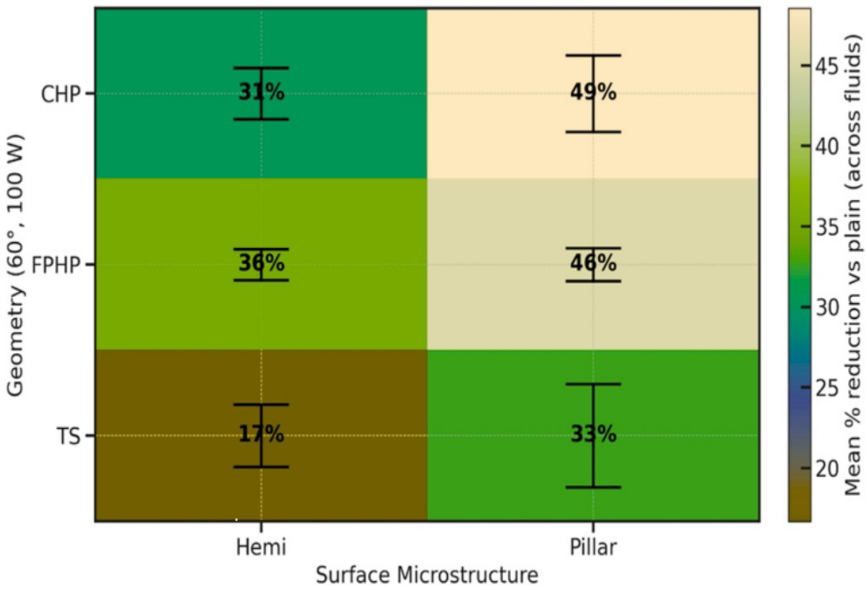

Figure 18. Microstructure effectiveness matrix (60°, 100 W)

DI baseline. Sensitivity of the interpolated field to sensor placement and interpolation method was acknowledged. Interpretation was therefore focused on relative suppression magnitude rather than exact peak location.

Figure 19 shows the micropillar surface with graphene–water removing localized hot ridges that persisted on the plain–DI plate. The interpolated field for the baseline case exhibited a center-weighted hotspot near the heater block with a peak roughly 3.5°Cabove the field mean. The micropillar–graphene field compressed this spread to about 0.9°C, a reduction of ~74%. The tighter contours indicated thinner and more uniformly replenished microlayers at the evaporator–fluid interface. The pillars introduced contiguous capillary pathways that advected cool liquid toward the heater footprint and evacuated vapor uniformly, thereby suppressing long residence times for microbubbles and limiting local superheat. Graphene–water further conditioned the surface, increasing the thermal conductance of the interfacial layer and facilitating rapid nucleation at lower wall temperatures (Sethuraman et al., 2024). The remaining weak gradients in the optimized map likely reflected macroscopic spreading resistance rather than local boiling limits. This change in spatial uniformity was significant for subsequent tests that increased power or modulated angle, as smaller temperature non-uniformity reduced the likelihood of initiating a dry patch that could propagate across the plate during transients. It also implied lower thermomechanical stress in bonded interfaces and soldered joints, thereby extending the reliability of electronics modules mounted directly above the evaporator. In comparative evaluations, hotspot suppression would result in a later onset of temperature-based throttling for CPUs or power devices, allowing for a higher sustainable power density at identical noise and coolant flow conditions, while maintaining a margin against condenser-side perturbations.

Persistence under long-term cycling and fouling was not claimed as proven. Short-term stability screens were reported, but long-duration durability was positioned as required follow-on work. This boundary was stated explicitly to avoid overextension of the thermal-field result.

Figure 20 (a) Unit-cell geometry definition for capillary-lane curvature scale $r_{eff} \approx (p - d)/2$ and wetted-sidewall contribution; (b) estimated wetted-area amplification A_{wet}/A_{proj} for plain, hemispherical, and micropillar textures; (c) normalized capillary-pressure scaling $\Delta P_{cap}/(2\gamma)$ versus cosθfor representative r_{eff} values; (d) measured R_{th} at 100 W versus estimated A_{wet}/A_{proj} for the three surface classes

Figure 20 presents the comparative behavior of microstructured evaporators when capillary supply and interfacial area are cast into geometry-based scaling parameters. Figure (a) illustrates a square-

 https://doi.org/10.37819/nanofab.2025.0019

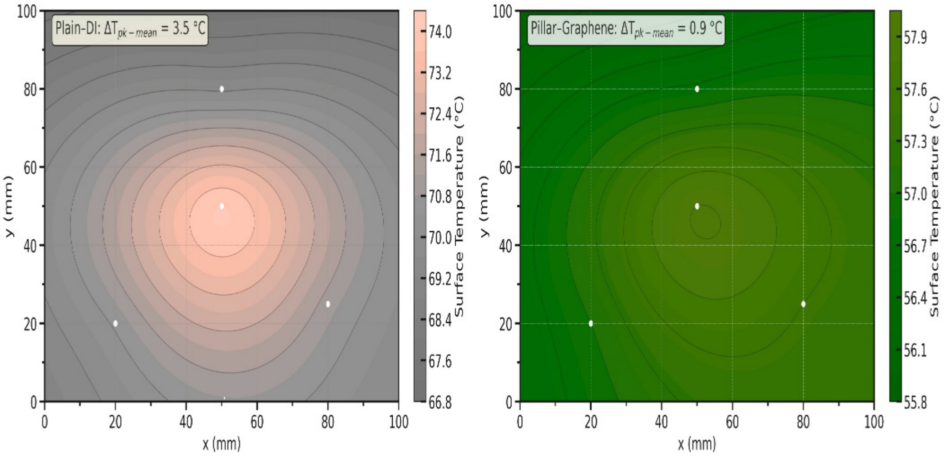

Figure 19. 2D temperature field on the flat plate evaporator

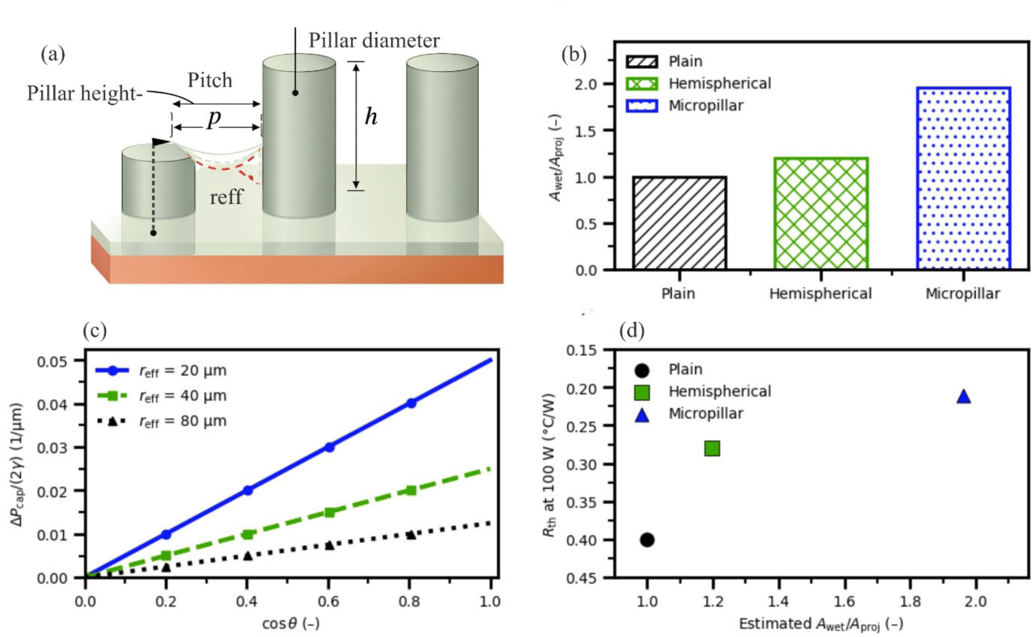

Figure 19.

lattice unit cell in which pitch p, diameter d, and height hdefine both the inter-feature lane size $g = p - d$ and the curvature scale r_{eff}, so that capillary suction is expected to increase as the lane narrows and as wetting strengthens. Figure (b) shows that A_{wet}/A_{proj} increases from the plain baseline near unity to a modest amplification for hemispherical texturing and to the largest amplification for micropillars, so that larger interfacial area is made available for evaporation and microlayer conduction when sidewalls are introduced. Figure (c) shows a linear dependence of $\Delta P_{cap}/(2\gamma)$on cosθand an inverse dependence on r_{eff}, *so t*hat a more hydrophilic state and a smaller curvature scale are jointly required for large capillary driving pressure. The slopes indicate that, at fixed wetting, halving r_{eff}doubles the normalized capillary pressure, so that pitch control is predicted to be a strong design lever. Figure (d) relates these scalings to the measured outcome at 100 W, where the experiment showed a reduction i*n* R_{th} *f*rom the plain point to the hemispherical point and a further reduction to the micropillar point, consistent with a mechanism in which both effective wetted area and replenishment capability govern sustained thin film boiling. These coupled trends suggest that the widening performance separation at higher heat flux can be mechanistically supported by geometry-driven increases in capillary headroom and wetted area, while the persistence of enhancement across conditions can be interpreted through the combined roles of wetting state (cosθ) and lane curvature scale (r_{eff}), as requested for explicit mechanism linkage

4. CONCLUSION

This work evaluated stability-qualified graphene, CuO, Al_2O_3, and TiO_2 nanofluids on plain, hemispherical, and micropillar copper evaporators integrated into a circular heat pipe, a flat-plate heat pipe, and a wickless thermosyphon under controlled cooling at 25.0 ± 0.2 °C and inclinations of 0°–90°. Surface metrology and wettability measurements were completed, and dispersions were screened by DLS, zeta potential, UV–Vis retention, viscosity, and thermal conductivity before and after the thermal campaign. For the circular device at 60°, the micropillar texture increased the apparent evaporator heat-transfer coefficient from 1,980 to 3,780 W m^{-2} K^{-1} at 100 W and from 990 to 1,760 W m^{-2} K^{-1} at 20 W, confirming a sustained high-flux advantage. Hemispherical texturing yielded 2,835 W m^{-2} K^{-1} at 100 W, consistent with nucleation activation without continuous capillary lanes. Orientation effects were small for wicked devices, while the thermosyphon shifted from ~0.18 °C/W at 90° to ~1.0 °C/W at 0° at 100 W, and an orientation sensitivity index of 0.35 ± 0.05 for plain DI water was reduced to ~0.22 when micropillars and graphene were applied. Graphene retained 96% UV–Vis absorbance at 24 h, reached $\zeta = -42$ mV, and stayed within a 10% viscosity rise, supporting repeatable operation across the test matrix. These results establish that capillary replenishment, wetted-area amplification, and interfacial conditioning govern performance gains under passive operation in practice. Future studies will quantify long-cycle durability, deposition evolution, and outdoor exposure effects, and will couple in-situ visualization with geometry-resolved models to link capillary pressure metrics to dry-out boundaries.

Conflict of interest: The author(s) declared no potential conflicts of interest.

Funding: No financial support was provided.

Availability of Data and Materials: The datasets used during the current study are available from the corresponding author on reasonable request.

Authors' Contributions: Conceptualization, Wasurat Bunpheng; Methodology, V. M. Rajavel Muthaiah and Ratchagaraja Dhairiyasamy; Investigation, Wasurat Bunpheng and Choon Kit Chan; Data Curation, Ratchagaraja Dhairiyasamy; Formal Analysis, Choon Kit Chan and V. M. Rajavel Muthaiah; Writing – Original Draft, Wasurat Bunpheng; Writing – Review & Editing, V. M. Rajavel Muthaiah and Choon Kit Chan; Visualization, Wasurat Bunpheng and Ratchagaraja Dhairiyasamy; Supervision, V. M. Rajavel Muthaiah; Project Administration, V. M. Rajavel Muthaiah; Resources, Choon Kit Chan.

REFERENCES

Aljaafari, H. A. S., Sultan, A. J., Sabri, L. S., Sawaran Singh, N. S. S., Hashemi-Karouei, S. H. H., Jasim, D. J., Alinia-Kolaei, M., & Sheshpoli, F. S. (2025). Numerical investigation of the effect of external helical fins reinforced with rectangular fins on improving convective heat transfer in helical coils. *International Journal of Thermofluids*, *29*. https://doi.org/10.1016/j.ijft.2025.101345

Aytaç, İ., Khanlari, A., Tuncer, A. D., Variyenli, H. İ., & Ünvar, S. (2024). Performance improvement of a heat pipe evacuated solar water collector using quartz/water nanofluid: A numerical and experimental study. *Renewable Energy*, *236*. https://doi.org/10.1016/j.renene.2024.121423

Balan, V., Ramakrishnan, S., Palani, G., & Selvaraju, M. (2024). Investigation on the Enhancement of Heat Transferin Counterflow Double-pipe Heat Exchangerusing Nanofluids. *Thermal Science*, *28*(1A), 233–240. https://doi.org/10.2298/TSCI230312273V

Chakraborty, M., & Chakraborty, S. (2025). Implications of Raychaudhuri equation and geodesic focusing in interacting two fluid systems. *European Physical Journal C*, *85*(1), Article 114. https://doi.org/10.1140/epjc/s10052-025-13850-6

Chan, C. K., Riaz, M. B., Rehman, A. U., Ewe, L. C., & Sarwar, L. (2024). Dynamics of Jeffrey fluid flow and heat transfer: A Prabhakar fractional operator approach. *International Journal of Thermofluids*, *22*, Article 100709. https://doi.org/10.1016/j.ijft.2024.100709

Chaudhari, V., Dharmadhikari, M., & Kolhe, V. (2024). Experimental Analysis of Thermal Performance for Heat Pipe Heat Exchanger with ZnO Nanofluid. *Letters in Applied NanoBioScience*, *13*(2). https://doi.org/10.33263/LIANBS132.080

Darvesh, A., Boukhris, I., Collantes Santisteban, L. J., Al-Buriahi, M. S., Elqahtani, Z. M., Akgül, A., García, L. K. O., & Hassani, M. K. (2025). Radiative heat transfer in MHD copper-based polymer nanofluid over a sphere using larger radius and inter particle spacing of nanoparticles. *Results in Engineering*, *26*. https://doi.org/10.1016/j.rineng.2025.105012

Dhairiyasamy, R., Murugesan, M., Mahendren, S., Saleh, B., Varshney, D., & Singh, S. (2025). Enhanced heat transfer in copper heat pipes using hybrid nanofluids: experimental and RSM analysis. *Digest Journal of Nanomaterials and Biostructures*, *20*(1), 287–300. https://doi.org/10.15251/DJNB.2025.201.287

Elumalai, S., & Kadamban, M. (2025). Heat transfer optimization using silver nanoparticle-stabilized nanofluids in copper heat pipes: comparative analysis of stabilizing agents. *Engineering Research Express*, *7*(1). https://doi.org/10.1088/2631-8695/ada5ad

Gao, Y., Chen, B., Wu, D., Dai, Z., Wang, C., & Zhang, X. (2022). Comparative study of various solar power generation systems integrated with nanofluid-flat heat pipe. *Applied Energy*, *327*. https://doi.org/10.1016/j.apenergy.2022.120052

Govindasamy, M., Ezhumalai, M., Dhairiyasamy, R., Varshney, D., Singh, S., & Gabiriel, D. (2025). Comprehensive Investigation into the Thermal Performance of Nanofluid-Enhanced Heat Pipes for Advanced Thermal Management Systems. *Eng*, *6*(3). https://doi.org/10.3390/eng6030055

Hu, Y., Meng, G., Yao, Y., Zhang, F., & Luoshan, M. (2025). Experimental investigation on the start-up and thermal performance of nanofluid-based pulsating heat pipe. *Applied Thermal Engineering*, *259*. https://doi.org/10.1016/j.applthermaleng.2024.124897

Inn, L. Q., Oumer, A. N., Azizuddin, A. A., Parlaungan Siregar, J. P., & Cionita, T. (2023). Numerical Analysis of Battery Thermal Management System of Electric Vehicle. *Journal of Advanced Research in Numerical Heat Transfer*, *13*(1), 106–114. https://doi.org/10.37934/arnht.13.1.106114

Jin, Z., Chen, Y., Mu, J., & Chen, C. (2025). Heat transfer characteristics of graphene oxide nanofluids suction core heat pipes. *Huaxue Gongcheng Chemical Engineering China*, *53*(3), 46–82. https://doi.org/10.3969/j.issn.1005-9954.2025.03.008

K, S. K., Arunkumar, M., Ravi, S., Gupta, D., Rajan, K., Dhairiyasamy, R., Mohanavel, V., Subbiah, R., & Soudagar, M. E. M. (2025). Improving the thermal efficiency of a solar water heater by using PCM with copper powder (Cu), silicon carbide (SiC), and boron nitride (BN) nano particles. *Results in Engineering*, *27*. https://doi.org/10.1016/j.rineng.2025.105952

Kadhim, S. A., Abdul-Ghafoor, Q. J., Hammoodi, K. A., Abdul wahhab, H. A., Ibrahim, O. A. A.-M., & Al-Ghezi, M. K. S. (2025). Enhancement of the heat transfer performance of a double-pipe heat exchangers in various configurations using Al_2O_3 nanofluid: A focused review. *Journal of Thermal Analysis and Calorimetry*, *150*(6), 3941–3965. https://doi.org/10.1007/s10973-025-14042-w

Kadirgama, G., Ramasamy, D., Kadirgama, K., Samylingam, L., Kok, C. K., Aslfattahi, N., Schmirler, M., Chalak Qazani, M. R., & Yusaf, T. (2025). Characterization and machine learning analysis of hybrid alumina-copper oxide nanoparticles in therminol 55 for medium temperature heat transfer fluid. *Scientific Reports*, *15*(1). https://doi.org/10.1038/s41598-025-92461-3

Kalbande, V. P., Walke, P. V., Untawale, S., & Mohan, M. (2022). Performance Evaluation of Novel Heat Pipe-Assisted Thermal Storage System with Parabolic Trough Solar Collector Using Nanofluid. *Energy Technology*, *10*(9). https://doi.org/10.1002/ente.202200118

Khan, I., Alharthi, T. N., Khan, G., Alhamzi, G., Safdar, M., Jamil, B., Taj, S., Khan, R. A., & Koh, W. S. (2025). LIE SYMMETRIES IN NONLINEAR LIQUID FILM FLOW WITH HEAT AND MASS TRANSFER AND VARIABLE MAGNETIC FIELD. *Fractals*. https://doi.org/10.1142/S0218348X25402492

Kumar, R., Dwivedi, A., & Goel, V. (2025). Performance estimation of nanofluids-charged oscillating heat pipe-assisted battery thermal management systems: An experimental analysis. *International Journal of Heat and Mass Transfer*, *247*. https://doi.org/10.1016/j.ijheatmasstransfer.2025.127201

Madadi, M., & Abbasian Arani, A. A. (2025). Experimental evaluation of photovoltaic thermal (PVT) system using a modular heat collector with flat back shape fins, pipe, nanofluids and phase change material. *Solar Energy Materials and Solar Cells*, *280*.

Mane, N. S., Hemadri, V., & Tripathi, S. (2025). Investigation of Effects of Vibrations on Nanofluid-Filled Pulsating Heat Pipe for Efficient Electric Vehicle Battery Thermal Management. *International Journal of Thermophysics*, *46*(1). https://doi.org/10.1007/s10765-024-03477-2

Muhammad, M., Shahmir, N., Alazman, I., Saleel, C. V. A., Asiri, J. M., Saeed, A. M., & Koh, W. S. (2025). Heat transfer performance appraisal of hybrid and ternary nanofluid flows over a wedge considering viscous dissipation and quadratic thermal convection: Non-similar solution approach. *Advances in Mechanical Engineering*, *17*(6). https://doi.org/10.1177/16878132251349955

Nallusamy, R., & Rathinasamy, S. (2025). Comparative analysis of nanoparticle-based nanofluids in heat pipes: enhancing thermal conductivity with graphene oxide, copper oxide, iron oxide, and titanium oxide. *Revista Materia*, *30*. https://doi.org/10.1590/1517-7076-RMAT-2024-0577

Naruka, D. S., Dwivedi, R., & Singh, P. K. (2025). Experimental Investigation to Elucidate the Temporal Effect of Nanofluids on the Thermal Performance of Heat Pipes. *Heat Transfer Engineering*, *46*(6), 542–553. https://doi.org/10.1080/01457632.2024.2325278

Saad, I., Maalej, S., & Zaghdoudi, M. C. (2022). Investigation of the Thermal Performance of a Nanofluid-filled Grooved Cylindrical Heat Pipe for Electronics Cooling. *Journal of Advanced Research in Fluid Mechanics and Thermal Sciences*, *99*(2), 135–154. https://doi.org/10.37934/arfmts.99.2.135154

Sethuraman, R., Muthuvelan, T., Mahadevan, S., & Dhairiyasamy, R. (2024). Maximizing Thermal Performance of Heat Pipe Heat Exchangers for Industrial Applications Using Silver Nanofluids. *International Journal of Thermophysics*, *45*(4). https://doi.org/10.1007/s10765-024-03343-1

Soudagar, M. E. M., Chaturvedi, R., Kulshreshta, A., Christy, J. H., Murali, M., Mohanavel, V., Mohana Krishnan, A., Gnanasekaran, L., & Manikandan, A. (2025). Hybrid PCM concentration on energy storage and thermal performance of solar thermal air heater featured with carbon nanotube and copper oxide nanofluid. *Applied Thermal Engineering*, *279*. https://doi.org/10.1016/j.applthermaleng.2025.127596

Thanikodi, T., Giri, J., Al-Lehaibi, M., Hourani, A. O., & Anderson, A. (2025). Performance enhancement of heat pipe-based solar tube collectors using graphene nanofluids: Experimental analysis and thermal optimization. *Case Studies in Thermal Engineering*, *73*. https://doi.org/10.1016/j.csite.2025.106460

Zhao, S., Xu, G., Wang, N., & Zhang, X. (2018). Experimental study on the thermal start-up performance of the graphene/water nanofluid-enhanced solar gravity heat pipe. *Nanomaterials*, *8*(2). https://doi.org/10.3390/nano8020072